Astronomy & Astrophysics manuscript no. VVV˙DR1 © ESO 2011
November 24, 2011

VVV DR1: The First Data Release of the Milky Way Bulge and Southern Plane from the Near-Infrared ESO Public Survey VISTA Variables in the Vía Láctea[⋆]

R. K. Saito[1], M. Hempel[1], D. Minniti[1,2,3], P. W. Lucas[4], M. Rejkuba[5], I. Toledo[6], O. A. Gonzalez[5], J. Alonso-García[1], M. J. Irwin[7], E. Gonzalez-Solares[7], S. T. Hodgkin[7], J. R. Lewis[7], N. Cross[8], V. D. Ivanov[9], E. Kerins[10], J. P. Emerson[11], M. Soto[12], E. B. Amôres[13,14], S. Gurovich[15], I. Dékány[1], R. Angeloni[1], J. C. Beamin[1], M. Catelan[1], N. Padilla[1,16], M. Zoccali[1,17], P. Pietrukowicz[18], C. Moni Bidin[19], F. Mauro[19], D. Geisler[19], S. L. Folkes[20], S. E. Sale[1,20], J. Borissova[20], R. Kurtev[20], A. V. Ahumada[9,21,22], M. V. Alonso[15,21], A. Adamson[23], J. I. Arias[12], R. M. Bandyopadhyay[24], R. H. Barbá[12,25], B. Barbuy[26], G. L. Baume[27], L. R. Bedin[28], A. Bellini[29], R. Benjamin[30], E. Bica[31], C. Bonatto[31], L. Bronfman[32], G. Carraro[9], A. N. Chenè[19,20], J. J. Clariá[21], J. R. A. Clarke[20], C. Contreras[4], A. Corvillón[1], R. de Grijs[33,34], B. Dias[26], J. E. Drew[4], C. Fariña[27], C. Feinstein[27], E. Fernández-Lajús[27], R. C. Gamen[27], W. Gieren[19], B. Goldman[35], C. González-Fernández[36], R. J. J. Grand[37], G. Gunthardt[21], N. C. Hambly[8], M. M. Hanson[38], K. G. Hełminiak[1], M. G. Hoare[39], L. Huckvale[10], A. Jordán[1], K. Kinemuchi[40], A. Longmore[41], M. López-Corredoira[42,43], T. Maccarone[44], D. Majaess[45], E. L. Martín[46], N. Masetti[47], R. E. Mennickent[19], I. F. Mirabel[48,49], L. Monaco[9], L. Morelli[29], V. Motta[20], T. Palma[21], M. C. Parisi[21], Q. Parker[50,51], F. Peñaloza[20], G. Pietrzyński[18,19], G. Pignata[52], B. Popescu[38], M. A. Read[8], A. Rojas[1], A. Roman-Lopes[12], M. T. Ruiz[32], I. Saviane[9], M. R. Schreiber[20], A. C. Schröder[53,54], S. Sharma[20,55], M. D. Smith[56], L. Sodré Jr.[26], J. Stead[39], A. W. Stephens[57], M. Tamura[58], C. Tappert[20], M. A. Thompson[4], E. Valenti[5], L. Vanzi[16,59], N. A. Walton[7], W. Weidmann[21], and A. Zijlstra[10]

(Affiliations can be found after the references)

Received ; Accepted

ABSTRACT

Context. The ESO Public Survey VISTA Variables in the Vía Láctea (VVV) started in 2010. VVV targets 562 sq. deg in the Galactic bulge and an adjacent plane region and is expected to run for $\sim$ 5 years.

Aims. In this paper we describe the progress of the survey observations in the first observing season, the observing strategy and quality of the data obtained.

Methods. The observations are carried out on the 4-m VISTA telescope in the $ZYJHK_\mathrm{s}$ filters. In addition to the multi-band imaging the variability monitoring campaign in the K_s filter has started. Data reduction is carried out using the pipeline at the Cambridge Astronomical Survey Unit. The photometric and astrometric calibration is performed via the numerous 2MASS sources observed in each pointing.

Results. The first data release contains the aperture photometry and astrometric catalogues for 348 individual pointings in the $ZYJHK_\mathrm{s}$ filters taken in the 2010 observing season. The typical image quality is $\sim 0\farcs9 - 1\farcs0$. The stringent photometric and image quality requirements of the survey are satisfied in 100% of the JHK_s images in the disk area and 90% of the JHK_s images in the bulge area. The completeness in the Z and Y images is 84% in the disk, and 40% in the bulge. The first season catalogues contain 1.28×10^8 stellar sources in the bulge and 1.68×10^8 in the disk area detected in at least one of the photometric bands. The combined, multi-band catalogues contain more than 1.63×10^8 stellar sources. About 10% of these are double detections due to overlapping adjacent pointings. These overlapping multiple detections are used to characterise the quality of the data. The images in the JHK_s bands extend typically $\sim$ 4 mag deeper than 2MASS. The magnitude limit and photometric quality depend strongly on crowding in the inner Galactic regions. The astrometry for $K_s = 15 - 18$ mag has $rms \sim 35 - 175$ mas.

Conclusions. The VVV Survey data products offer a unique dataset to map the stellar populations in the Galactic bulge and the adjacent plane and provide an exciting new tool for the study of the structure, content and star formation history of our Galaxy, as well as for investigations of the newly discovered star clusters, star forming regions in the disk, high proper motion stars, asteroids, planetary nebulae, and other interesting objects.

Key words. Galaxy: bulge – Galaxy: disk – Galaxy: stellar content – Stars: abundances – Infrared: stars – Surveys

1. Introduction

The VISTA Variables in the Vía Láctea (VVV) Survey is mapping 562 square degrees in the Galactic bulge and the southern disk in the near-infrared (Minniti et al. 2010). The VVV Survey gives near-IR multi-colour information in five passbands: Z (0.87 μm), Y (1.02 μm), J (1.25 μm), H (1.64 μm), and K_s (2.14 μm), as well as time coverage spanning over 5 years, that will complement past/recent, current and upcoming surveys such as 2MASS, DENIS, GLIMPSE-II, VPHAS+, MACHO, OGLE, EROS, MOA, PLANET, and GAIA.

VVV is an ESO Public Survey, i.e., the observational raw data are made available to the astronomical community imme-

---

Send offprint requests to: R. K. Saito: rsaito@astro.puc.cl

[⋆] Based on observations taken within the ESO VISTA Public Survey VVV, Programme ID 179.B-2002 diately, whereas the reduced data will be published once a year in a Data Release through ESO. This paper describes and characterises the first data release (DR1) of the VVV Survey. Some first results of the VVV Survey based on early science images taken in the bulge and disk fields are highlighted in Saito et al. (2010) and Catelan et al. (2011).

The preparatory phase for the VVV Survey started in 2006, with the first test observations obtained in October 2009. Regular operations started with the first survey observations in February 2010. The data collected during the first year of observations until October 2010 are the subject of this public release. Our survey is planned to be carried out for 5 years, and we expect to produce yearly accumulated data releases.

The VVV Survey is foremost a variability study of the inner regions of the Milky Way (Minniti et al. 2010), but will also complement the existing 2MASS JHK photometry (Cutri et al. 2003), extending to much fainter limits while adding two additional filters (ZY), and providing time domain information useful for variability and proper motion studies. In particular, the higher resolution of the VVV data represents a huge advantage in crowded fields in relation to previous near-IR surveys such as 2MASS and DENIS (Epchtein et al. 1994), where the single-epoch photometry was confusion-limited, reaching $K_s \sim 14.3$ mag. The limiting magnitude of the VVV data using aperture photometry is $K_s \sim 18.0$ mag in most fields. Even in the innermost fields ($|b| \leq 1°$) the VVV Survey reaches $K_s \sim 16.5$ mag, at least a magnitude deeper than the IRSF/SIRIUS Survey of the Galactic Centre (Nagayama et al. 2003; Nishiyama et al. 2006, 2009).

The VVV Survey was designed to complement the UKIDSS-GPS (Lucas et al. 2008), VPHAS+ (see Arnaboldi et al. 2007), and the GLIMPSE-II surveys (Benjamin et al. 2003). The UKIDSS-GPS is mapping $|b| < 5°$ in Galactic latitude in the northern plane for 3 epochs, while VPHAS+ also observes the Galactic plane in the optical and Hα using the ESO VLT Survey Telescope (VST).

GLIMPSE-II survey images the central $\pm 10°$ of the plane in 4 bands with IRAC. VVV provides variability information for the overlap region, supporting studies of the content and distribution of stars, stellar populations, and interactions of the strong nuclear wind with the ambient ISM above and below the nucleus, as well as the rate and location of current star formation.

Multiband *Spitzer* public surveys with IRAC (mid-IR at 3.6 μm, 4.5 μm, 5.6 μm and 8.0 μm) and MIPS (far-IR, 23.7 μm, 71.4 μm weighted average wavelength), respectively, cover the mid-plane ($|b| < 1°$) at $65° < l < 10°$ and $-10° < l < -65°$. The southern half of these surveys overlaps with the VVV disk area, allowing the detection and characterisation of star formation regions and to probe the structure of the inner disk of the Galaxy. In optically obscured regions the IRAC data complement both the VVV Survey and the VST/VPHAS+ by tracing the influence of the most massive stars on star formation.

In addition, we complement the existing bulge microlensing surveys such as MACHO (Alcock et al. 2000) and OGLE (Udalski et al. 1993), which observe in optical bands, with limited or no colour information. These surveys mostly concentrate on regions of low extinction. VVV will provide useful variability information for the overlap regions.

The data are of excellent quality in general, and only a small fraction did not pass our quality controls and had to be reacquired. These DR1 data have passed all the initial quality controls as performed by the survey team in collaboration with the Cambridge Astronomical Survey Unit (CASU)[1]. We checked image defects, telescope problems, seeing, zero point, magnitude limit, ellipticity and airmass, for instance. However, it is important to stress that the data quality and calibrations will improve with subsequent data releases.

Here we will address the general information for the community, e.g., on the survey area and strategy, data quality, progress in the observations, published source lists, as well as examples of specific applications. In addition, the data, procedures and additional information are available through the ESO Archive[2], the VVV Survey Science Team homepage[3], CASU, and through the VISTA Science Archive (VSA) webpage[4].

This paper is organized as follows:

Section 2 describes the area coverage and the observations with VISTA as well as the data processing. Section 3 describes the photometric quality (limits, accuracy), as well as completeness. Section 4 discusses a comparison with 2MASS. Section 5 presents a comparison between the VVV DR1 (aperture) catalogues and PSF photometry. Section 6 describes the astrometric data quality. Section 7 presents density maps for the bulge and disk fields. Section 8 describes a suitability test of the DR1 data for difference image analysis.

The final section summarizes and presents our conclusions, including important caveats regarding this DR1, and future improvements to be implemented in DR2. Finally, the VVV tile coordinates are listed in the Appendix.

2. Survey Area and Observations

2.1. Telescope and Instrument

The telescope used to carry out the VVV Survey is VISTA (Visible and Infrared Survey Telescope for Astronomy), a 4-m class wide-field telescope with a single instrument, VIRCAM (VISTA InfraRed CAMera; Dalton et al. 2006; Emerson & Sutherland 2010), located on its own peak at ESO's Cerro Paranal Observatory in Chile, about 1500m away from the VLT. Its primary mirror has a diameter of 4.1m, providing a $f/3.25$ focal ratio at the Cassegrain focus where the instrument is mounted. The secondary mirror has a 1.24m diameter. The start of survey operations of the telescope was on April 1, 2010, but most VISTA surveys, including VVV, started collecting science observations a few months earlier, in parallel with the last phases of the scientific performance verification and operations fine-tuning performed by Paranal Observatory staff. During the first year of operations the mirrors were coated with silver, which is optimized for near-IR observations.

With 1.64 deg diameter VIRCAM offers the largest unvignetted field of view in the near-IR regime on 4-m class telescopes. It is equipped with 16 Raytheon VIRGO 2048×2048 pixels^2 HgCdTe science detectors, with $0\farcs339$ average pixel scale. Each individual detector therefore covers $\sim 694 \times 694$ arcsec^2 on the sky. The achieved image quality (including seeing) is better than $\sim 0\farcs6$ on axis. The image quality distortions are up to about 10% across the wide field of view. The detectors are arranged in a 4×4 array, with large spacings of 90% and 42.5% of the detector size along the X and Y axes, respectively. A single pointing, called a pawprint, covers 0.59 sq. deg, and provides partial coverage of the field of view. By combining

---

[1] `http://casu.ast.cam.ac.uk/vistasp/`

[2] `http://www.eso.org/sci/archive.html`

[3] `http://vvvsurvey.org`

[4] `http://horus.roe.ac.uk/vsa/index.html`

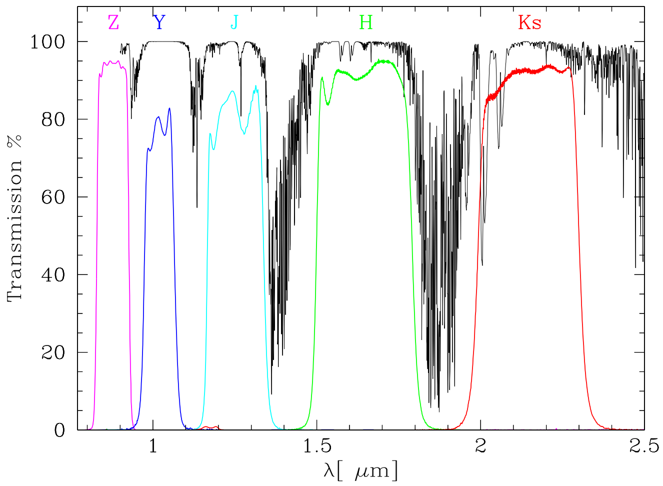

Fig. 1. Transmission curves for the five broad band filters present at the VIRCAM: Z, Y, J, H and K_s, compared with the typical atmospheric transmission profile for airmass = 1.0 and 1.0 mm water vapour. The effective wavelengths for all filters are listed in Table 1.

Table 1. Effective wavelengths for the VISTA filter set used in the VVV observations and the relative extinction for each filter based on the Cardelli et al. (1989) extinction law (from Catelan et al. 2011).

Filter	$\lambda_{\text{eff}}(\mu m)$	A_X/A_V	$A_X/E(B-V)$
Z	0.878	0.499	1.542
Y	1.021	0.390	1.206
J	1.254	0.280	0.866
H	1.646	0.184	0.567
K_s	2.149	0.118	0.364

Table 2. VVV Survey completion in the 2010 season.

Tile type	Completed Tile	Total Tiles	Completion percentage
	Bulge		
JHK_s	188	196	95%
ZY	78	196	40%
Variability	113	5 × 196	12%
	Disk		
JHK_s	152	152	100%
ZY	128	152	84%
Variability	547	5 × 152	72%

6 pawprint exposures with appropriate offsets a contiguous coverage of a field is achieved with at least 2 exposures per pixel except at two edges. In all VISTA observations such a field is called a tile and covers a 1.64 sq. deg field of view. Throughout this paper we will use a tile as the individual exposure.

VIRCAM has four additional optical CCDs, two for guiding and two for active optics. For exposures longer than ∼ 40 sec the active optics is run in parallel mode with the observations. Due to VVV's very short individual exposures of (see Sec. 2.3) the active optics correction is only performed every ∼ 30 min or after a larger offset. This, combined with the need to survey the area fast (hence minimizing the overheads for more frequent active optics corrections), and typical seeing on Paranal limits the image quality obtained for the survey data to typically ∼ 0.9–1.0 arcsec (see Sec. 2.4).

VIRCAM is equipped with 5 broad-band filters (Z, Y, J, H, and K_s) and two narrow-band filters centred at 0.98 and 1.18 μm. The VVV Survey uses all 5 broad band filters spanning from 0.84 to 2.5 μm. Their effective wavelengths and relative extinctions are given in Table 1, while the transmission curves are shown in Fig. 1, compared to a typical atmospheric transmission profile for airmass 1.0 and 1mm water vapour in the atmosphere.

For more details about the telescope and instrument we refer to the VIRCAM instrument web pages[5], and the VISTA/VIRCAM User Manual (Ivanov & Szeifert 2009).

2.2. Survey area

The VVV Survey area consists of 348 tiles, 196 tiles in the bulge and 152 in the disk area. These two components were planned to cover 520 sq. deg, as follows: (i) the VVV bulge survey area covers 300 sq. deg between $-10° \leq l \leq +10°$ and $-10° \leq b \leq +5°$; and (ii) the VVV disk survey area covers 220 sq. deg between $295° \leq l \leq 350°$ and $-2° \leq b \leq +2°$. However, in order to maximize the efficiency of the tilling process (see Section 2.3), the Survey Area Definition Tool (SADT; Hilker et al. 2011) produced some shifts at the edges of the survey area, and as the result an area of ∼562 sq. deg (42 sq. deg larger) was observed. Thus, the observed area is within $-10.0° \lesssim l \lesssim +10.4°$ and within $-10.3° \lesssim b \lesssim +5.1°$ in the bulge, and $294.7° \lesssim l \lesssim 350.0°$ and $-2.25° \lesssim b \lesssim +2.25°$ in the disk. The VVV Survey area and tile numbering are shown in Fig. 2, while the list of all tile centres in Equatorial and Galactic coordinates is given in Table A.1. The tile names start with "b" for bulge and "d" for disk tiles, followed by the numbering shown in Fig. 2.

While the whole area was observed in the JHK_s, 95% of these tiles satisfy the stringent photometric and image quality parameters and are classified as completed. In the ZY bands the completion is somewhat lower, with 59% completed tiles. The tiles completed in the first season (until October 26, 2010) can be seen in Figs. 3, 4 and 5, respectively for ZY, JH, and K_s. Figure 5 also includes the tiles with at least one epoch observed during the variability campaign in the K_s band.

In the first season of the variability campaign 22 tiles in the disk area had 5 K_s epochs taken, while the majority had one or more additional K_s epochs completed. The completion rates individually for the bulge and disk areas are given in Table 2. Table A.1 states for each tile whether the observations in a given filter are completed, and how many additional K_s epochs were obtained until October 26, 2010.

Figure 6 shows cumulative distributions of image quality and airmass for the observed tiles in the 2010 season. The median image quality in the J, H and K_s filters is better than $0.''9$ as measured on combined tile images, while it is close to $1.''0$ for the Z and Y filters.

---

[5] `http://www.eso.org/sci/facilities/paranal/instruments/vircam/`

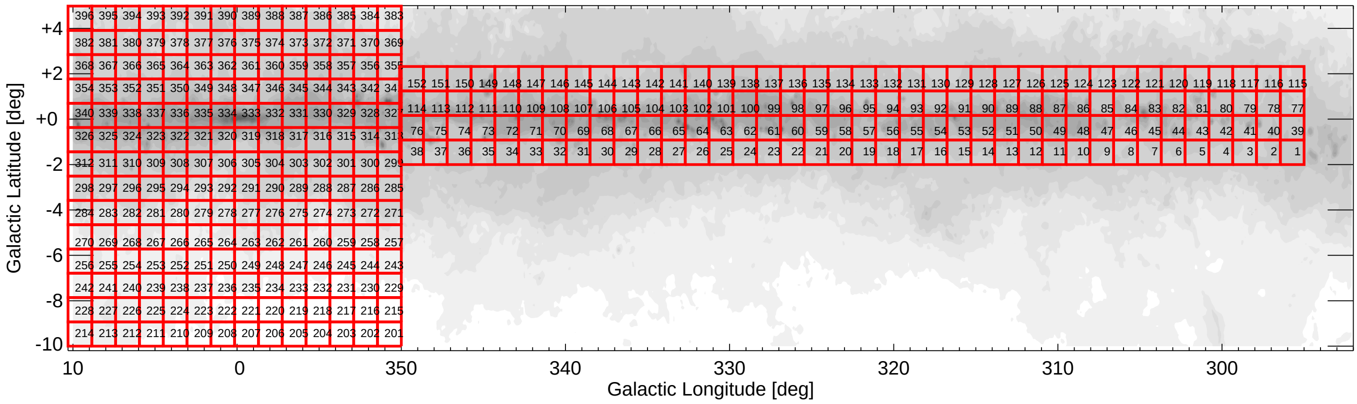

Fig. 2. VVV Survey area and tile numbering. The tile names start with "b" for bulge and "d" for disk tiles, followed by the numbering as shown in the figure. The centre coordinates for all VVV tiles are listed in Table A.1.

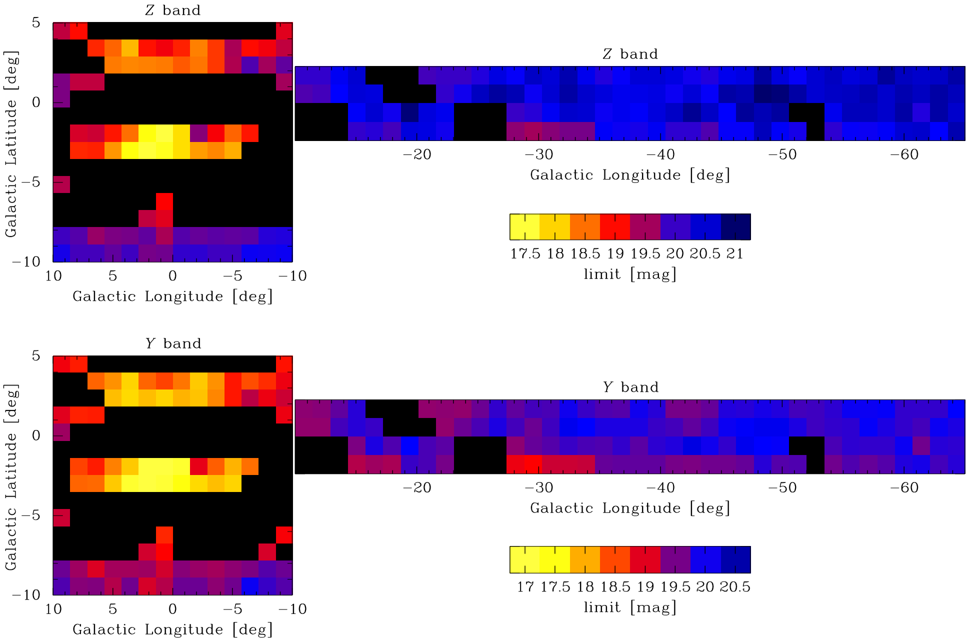

Fig. 3. The 5σ magnitude limits of the catalogues in the Z (top panel) and Y bands (bottom panel). The colour scale is shown in each case. The completeness of the DR1 can be also checked in the maps, where the missing tiles appear in black. Exposure times in the bulge and disk fields are different (see Table 3), which contributes the disk fields to have deeper photometry. Similar maps for J, H and K_s photometry, as well as for the variability campaign, are presented in Figs. 4 and 5.

2.3. Observing strategy

The first observations collected for the VVV Survey were taken during the VISTA science verification period in October 2009 when one field in the Galactic bulge at α=18:02:58.872, δ = −28:36:59.04 (J2000) was observed in the $ZYJHK_s$ filters (called SV field). In addition to the nearly-simultaneous multi-band images of the SV field, 11 K_s band exposures were taken to test the variability observing strategy. To establish the necessary number of exposures for proper sky subtraction, depending on crowding and number of resolved objects in the field, three additional tiles were observed in the K_s band, two bordering directly on the SV field and one at an offset position ≈1° south of the science target. Based on these early observations we adjusted the observing strategy, which differs slightly between the bulge and disk fields (i.e., with respect to exposure time, number of co-added exposures, and combination of tiles for sky subtraction).

Like all VISTA observations the VVV Survey is carried out in Service Mode. The basic observational unit is the so-called OB (observation block). The multi-filter, single-epoch OBs have been split into JHK_s and ZY OBs. The variability monitoring OBs have only single filter: K_s. OBs for two, three or four tiles were executed back-to-back to ensure that a sufficient number of

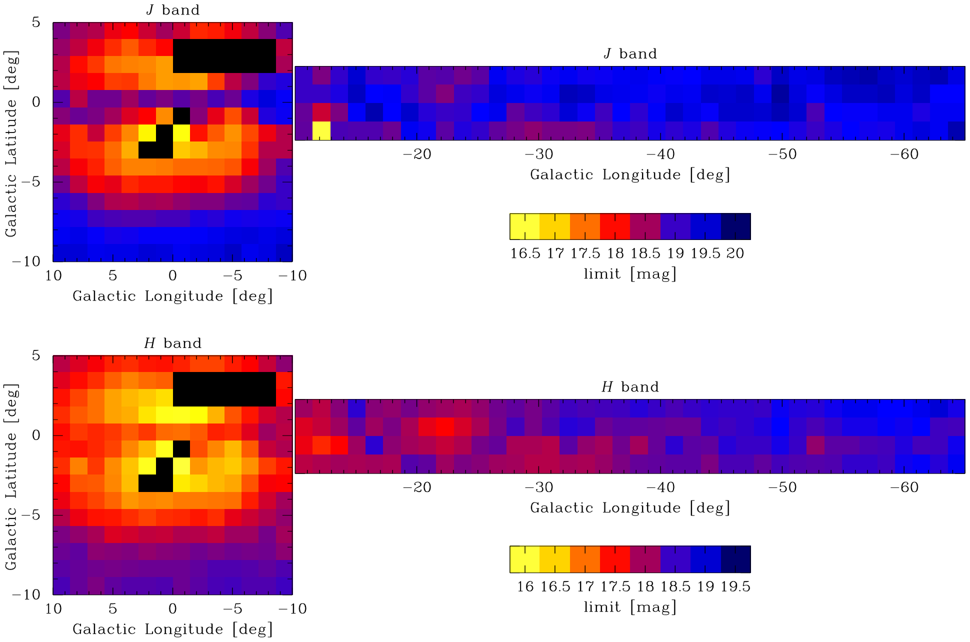

Fig. 4. The 5σ magnitude limits of the catalogues in the J (top panel) and H bands (bottom panel). The notation is similar to that presented in Fig. 3.

Table 3. Observing strategy and exposure times for VVV OBs.

Area	Filter	DIT[a] (s)	NDIT[b]	Median exp. time per pixel (s)
Bulge	Z, Y	10	1	40
Bulge	J	6	2	48
Bulge	H, K_s	4	1	16
Bulge	K_s (var)	4	1	16
Disk	Z, Y	20	1	80
Disk	J, H, K_s	10	2	80
Disk	K_s (var)	4	1	16

[a] Detector Integration Time
[b] Number of DITs

offset images were taken for each filter to create a high quality background sky frame.

The definition of the survey area was done with the help of the SADT, which provides the tile centres, guide and active optics stars, necessary for efficient execution of the survey OBs. Apart from the edges of the survey area, the input to SADT is also the tile pattern, which defines the large offsets that fill in the inter-detector gaps, as well as the size of the smaller (jitter) offsets that are executed at each of the 6 pawprint positions that together make a tile. All VVV OBs used the “Tile6n” pattern. In addition, at each of the 6 pawprint positions two smaller offsets are executed using the “Jitter2u” pattern. This means that in total, there are 12 exposures per filter, but given the large offsets, each pixel is covered by at least 4 exposures, except for the pixels along the y-edge of the tile (2 jitter positions and at least 2 pawprints). These, however, have overlaps with adjacent tiles. Therefore the complete survey area is covered by at least 4 exposures in each filter. Each image is a co-addition of NDIT exposures lasting DIT seconds each. The total exposure times for bulge and disk tiles are given in Table 3.

2.4. Data processing

VVV observations are pipeline processed within the VISTA Data Flow System (VDFS) pipeline at the CASU (Lewis et al. 2010). The processing is done on a night-by-night basis, and it consists of the following data reduction steps executed in the order described.

The mean dark current exposure, taken with the same DIT (integration time per exposure) and NDIT (number of coadds in the exposure) values, is subtracted from each image.

A linearity correction is applied for individual detectors using information on the readout time, exposure time and the reset image time. A “reset” exposure of 1.0s for every exposure is subtracted from each exposure within the data acquisition system, prior to writing the image to the disk.

The flat-field correction is done by dividing by a mean twilight flat-field image to remove small scale quantum efficiency variations and the large scale vignetting profile of the camera, as well as to normalize the gain of each detector to a common median value.

The sky background correction removes the large scale spatial background emission. Tests made with the science verification observations showed that 12 exposures (6 pawprint × 2 jitters) taken for each VVV tile do not yield good sky subtraction because of severely crowded fields, leaving “holes” at the positions of bright stars or very crowded regions with many overlapping stellar PSFs. Therefore for VVV a sky background map is produced by combining all exposures for a given filter taken within several concatenated OBs (tiles). Due to variability of the near-IR sky, the need to take at least 24 images with the same filter within $\sim$ 30 min poses limits to the exposure times for

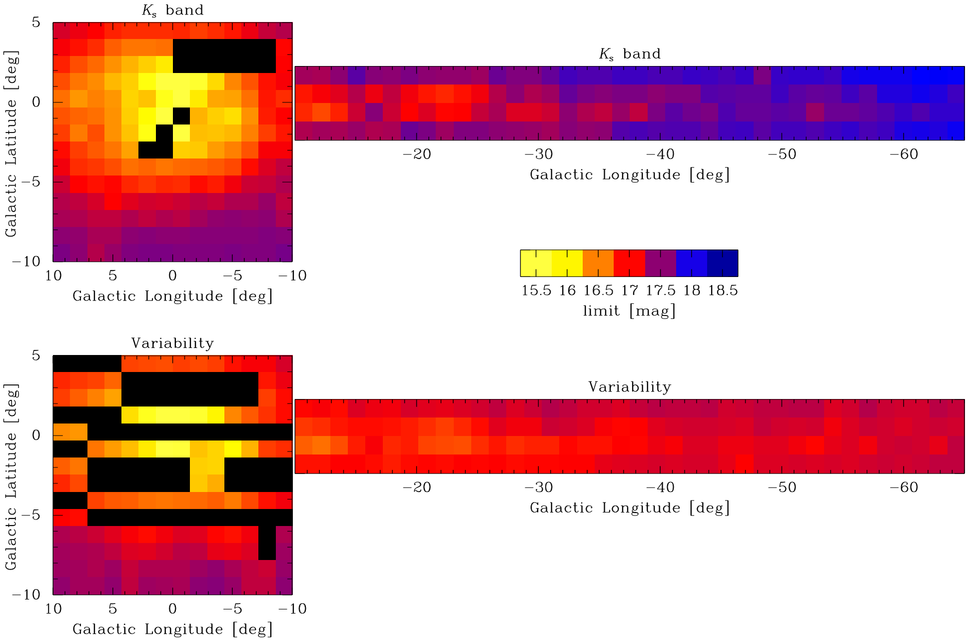

Fig. 5. The 5σ magnitude limit of the catalogues in the K_s band (top panel) and for the variability campaign (also performed in the K_s band, bottom panel). The colour scale is the same in both maps. Different strategies between the regular K_s observations and the variability campaign causes that in disk fields the variability data show shallower photometry. The notation is similar to that present in Fig. 3.

individual tiles and the number of different filters that can be included in each OB.

A "destriping correction" is performed by subtracting the low level horizontal stripe pattern introduced by the readout electronics of the VIRCAM detectors.

Jitter stacking is performed to align two slightly shifted images taken at a given pawprint position, combining them into a single image for each pawprint. The shifts are computed using the positions of many hundreds of stars detected in all images.

Object detection is performed for each stacked pawprint image. Positions, fluxes measured in several apertures of different sizes, and some shape measurements are written in the source catalogue. A flag indicates the most probable morphological classification, and in particular we note that "−1" is used to denote stellar objects, "−2" borderline stellar, "0" is noise, and "+1' is used for non-stellar objects. There also objects with flag "−7", denoting sources containing bad pixels, and the flag "−9" is used for saturated stars. These flags are derived mainly based on curve-of-growth analysis of the flux (Irwin et al. 2004). Figure 7 shows colour-magnitude diagrams (CMDs) for a moderately crowded bulge field (b264), comparing the distribution of the high quality sources, with all the other flags. Relative numbers for each flag are also indicated in the figure. In addition to a catalogue with extracted sources a confidence map is also computed (see Fig. 8).

The six stacked pawprint images are combined into a single deep tile and the catalogue extraction step is repeated. Tile images contiguously sample about 1.5 × 1.1 sq. deg on the sky. Confidence maps are computed for each tile, relaying information on the different exposure times for pixels across the tile (Fig. 8). The exposure times depend on the size of the jitter offsets and the number of exposures that are combined into a tile. The confidence maps clearly show the areas of detectors affected by bad pixels, such as the large patch in detector 1 (lower left corner in the right panel of Fig. 8), several rows in detector 4 (lower right corner) and the upper third of detector 16 (upper right corner). After stacking several dithered exposures in the final tile, most of these bad pixels are not noticeable (left panel of Fig. 8), but the large bad area on detector 16 has larger errors in the illumination correction map. The sensitivity of that upper third of the detector is much worse at shorter wavelengths, and some offsets with respect to 2MASS calibration for the whole tile have been found in Z, Y and J bands. Offsets at longer wavelengths, in the H and K_s bands, are within the calibration errors.

The first year data release of the tile images, catalogues and confidence maps described here is version 1.1. Detailed information about this version of VISTA data products as well as a brief description of all issues encountered during data processing is available on the CASU web page [6].

2.4.1. Generation of multi-band catalogues

Currently the version 1.1 single band tile catalogues from CASU are matched by the VVV team members using the STILTS package (Taylor 2006) and a KD-Tree based algorithm (Gurovich et al. 2011, in prep.) that uses the Cross et al. (2011, in prep.) implemented source matching method for the VSA data. The matching is done using astrometrically corrected tiles and catalogues, allowing a 1.″0 offset between point sources to be considered a match. Nevertheless, tests have shown that over 90% of the stellar sources are matched within less than 0.″5, as expected from the astrometric accuracy of the catalogues (see Sec. 6).

After matching the single band catalogues, most of the spurious detections around bright stars are rejected. Unfortunately

---

[6] `http://casu.ast.cam.ac.uk/surveys-projects/vista/technical`

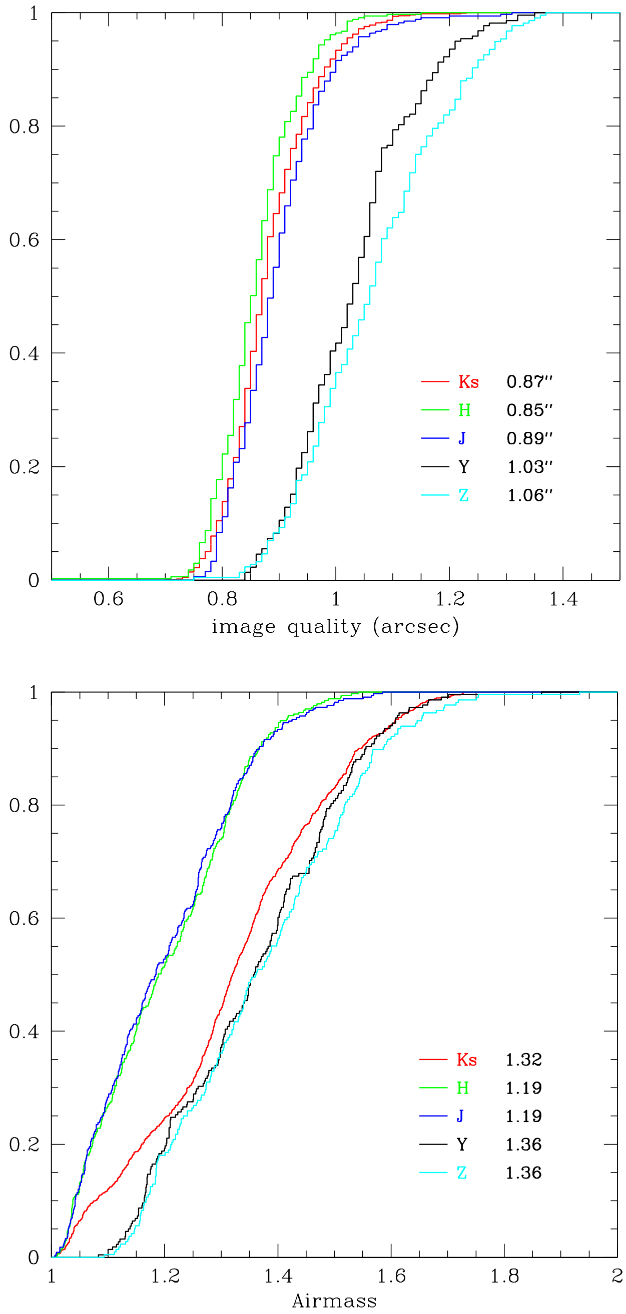

Fig. 6. Image quality and airmass cumulative distributions for the VVV observations obtained in 2010 in the $ZYJHK_s$ filters are plotted in the top and bottom panels, respectively. The median values of image quality and airmass for each filter are given in the legends.

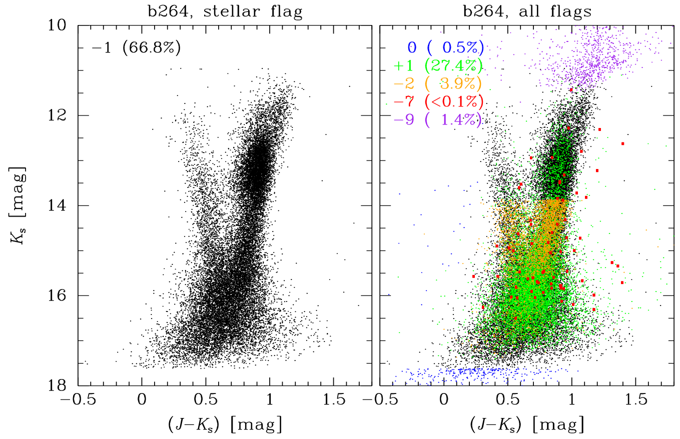

Fig. 7. K_s *vs.* $(J - K_s)$ CMDs for a moderately crowded bulge field (a section of tile b264), showing the high quality sources with −1, stellar flag (left panel), in comparison to all other flags found in the CASU catalogues (right panel). The relative number of sources is given in the top left corner.

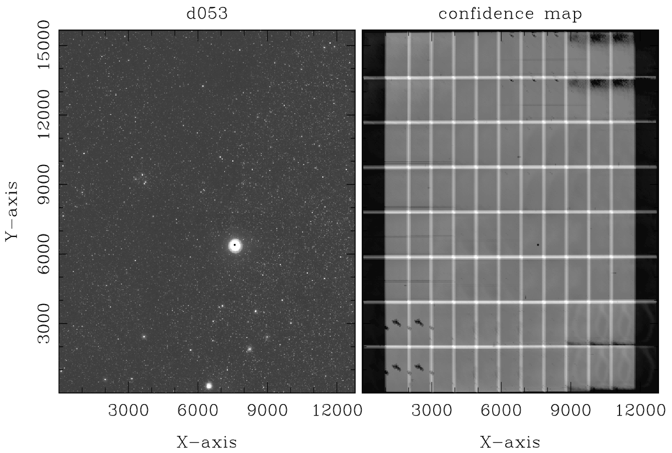

Fig. 8. The left panel shows the disk tile d053 in the K_s band, whereas its corresponding confidence map is shown in the right panel. The brighter regions in the confidence map have a longer total exposure time, due to the combination of the 6 pawprints. This image also includes 2 jitters at each pawprint position. Clearly visible in the lower left corner is a cluster of bad pixels (Chip 1). The six different positions correspond to the six pawprints, which are combined to fill the gaps between individual detectors.

the ellipticity sometimes varies from image to image; which then results in rejection of some sources which are only classified as "bona fide" stars in selected filters, but appear slightly more elongated, and are thus rejected as non-stellar, in other filters. A final multi-band catalogue contains ∼ 75 – 85% of the sources found in the catalogue with the least number of sources used for the matching, in general the K_s band, for low to intermediate extinction regions. Close to the Galactic plane high extinction affects more severely the source detection at short wavelengths, hence the source density is limited by the detection rate in the Y and Z bands. The comparison between the different tiles is hampered not only by the different median extinction values, but also by the strong extinction variation within any given tile. As an example, we divided two tiles (b305 and d003) into 0.25° × 0.25° sub-sections. Median extinction values A_V and their standard deviations are given in Table 4.

Multi-band catalogues corresponding to the DR1 data have also been generated by the VISTA Science Archive (VSA). While the single band DR1 data were already delivered through the ESO Archive, the multi-band catalogues will be publicly available in due time through the ESO Archive and VSA

Table 4. Galactic extinction values (median) for tiles b305 and d003, assuming $A_V = 3.1 \times E(B-V)$ and based on the prescriptions by (1) Schlegel et al. (1998), (2) Drimmel et al. (2003), (3) Amôres & Lépine (2005), (4) Marshall et al. (2006), (5) Froebrich et al. (2005), (6) Dobashi et al. (2005)

Tile	Reference	A_V (median)	$\sigma(A_V)$
b305	(1)	4.04	1.54
	(2)	4.81	1.81
	(3)	3.11	0.67
	(4)	3.95	1.22
	(5)	4.21	1.17
d003	(1)	5.73	2.05
	(2)	5.67	0.89
	(3)	3.25	0.91
	(4)	5.12	1.99
	(5)	2.66	0.66
	(6)	2.72	0.23

web page[7]. VSA will also provide multi-epoch catalogues for variable sources. Part of the data reduction and storage are performed using the Geryon cluster at the Center for Astro-Engineering at Universidad Católica (AIUC)[8].

3. Photometry

Photometric calibration of stacked pawprint images and tile images is done using numerous detected 2MASS stars. The calibration procedure follows closely that of WFCAM (Hodgkin et al. 2009). Internal photometric accuracy is of the order of ±2%, and for the J, H and K_s bands a similar accuracy as for 2MASS is achieved for most of the survey area. In particularly high extinction regions and for the Z and Y filters the photometric calibration errors are somewhat larger.

Figure 9 shows the photometric errors as a function of the magnitude computed by the CASU pipeline for the five passbands in a typical disk field (d003) as well as in an extreme case of a crowded bulge field close to the Galactic Centre (b305). Different extinction ($E(B-V)_{\rm d003} = 1.77$, $E(B-V)_{\rm b305} = 1.37$ mag; Schlegel et al. 1998) and crowding levels, as well as distinct observing strategies between disk and bulge areas (see Section 2.3), contribute to the shallower curves seen for the bulge data in all five passbands. The accuracy in the photometry can also be checked using the overlapping regions between the tiles. Figure 10 shows in the top panels the K_s photometry for stellar sources (also computed by the VDFS pipeline at CASU) in the overlapping area between tiles b305 and b291, and between d003 and d041. The 5σ magnitude limits reached for each passband, for both bulge and disk tiles as computed by the pipeline, are shown in Figs. 3, 4 and 5.

3.1. Saturation

VIRCAM detectors saturate at different levels, mostly around 33000 – 35000 ADU. Detector #5 has the smallest well depth (saturation at ~ 24000 ADU), but detector #13 has the largest non-linearity with of ~ 10% at 10000 ADU. This, combined with the rather bright near-IR sky results in a restricted dynamic range in the photometry.

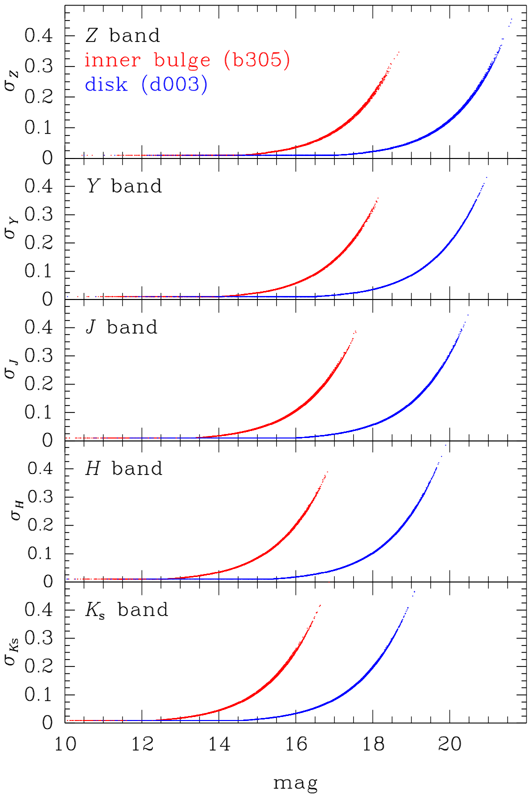

Fig. 9. Photometric error as a function of magnitude for each passband, $ZYJHK_s$, for a representative field in the disk (d003) and for a crowded bulge field close to the Galactic Centre (b305). We note that different exposure times between disk and bulge areas also contribute to the shallower curve for the bulge data.

Prior to reaching saturation VISTA detectors have nonlinear regime. Although linearity correction is performed in the pipeline data reduction, based on observations of an illuminated dome screen, for the stars close to the saturation limit there are still quite significant deviations with respect to 2MASS due to residual non-linearity. This can be seen clearly in Fig. 2 of Gonzalez et al. (2011a) and also in the VMC survey paper by Cioni et al. (2011).

The overlapping regions also help us to check the linearity of the photometry at the saturation limit. In the top panels of Fig. 10, for both bulge and disk data, part of the brightest stars slightly scatter from the linear distribution close to the saturation level, even taking into account that these are "−1" (stellar) sources in all VDFS single band catalogues from CASU. Some saturated stars are also present in the CASU catalogues (flagged as "−9", see Fig. 7), but these are not present in Fig. 10.

3.2. Photometric Completeness

Although the main goal of this paper is to describe the content of the first data release for the VVV Survey we want to demonstrate briefly how strongly the completeness of the source catalogues provided by CASU depends on the location of the selected area within the Survey.

---

[7] `http://horus.roe.ac.uk/vsa/index.html`

[8] `http://www.aiuc.puc.cl/`

To do so we carried out artificial star experiments, comparing the detection rate for artificial stars (AS) added to the images using the CASU source detection package *imcore* (Irwin et al. 2004). We selected two different tiles from the bulge area, namely b204 and b314, representing different levels of crowding. From these tiles we cut a small 2000 × 2000 pixel^2 area ($11.'3 \times 11.'3$) for the completeness tests. The two fields were centred on α_{2000}=18:12:13.173, δ_{2000}=-38:07:49.220 for b204 ($l, b = 354.72°, -9.37°$), and α_{2000}=17:29:28.920, δ_{2000}= -36:00:09.800 for b314 ($l, b = 352.21°, -0.92°$), respectively. The field b204 represents a less crowded section of the survey area, whereas b314, close to the Galactic Centre, is one of the most crowded fields. The K_s band source catalogues for the complete tile and the respective sub-sections contain $482,004/11,584$ (b204) and $1,137,615/23,691$ (b314) sources. We point out that in a preliminary test we applied the source detection package to the complete b204 tile and confirmed the number of sources obtained by the CASU pipeline, hence validating the source detection in the AS experiments.

In our completeness tests we added 5000 AS to the original images for 16 individual magnitude intervals, each 0.2 mag wide. The positions of these stars were chosen randomly, but the same positions and K_s magnitudes were used for both fields. To create the AS we derived a single point spread function (PSF), using isolated stars within the corresponding image. We leave the completeness test using a variable PSF for later. The AS images were constructed using the IRAF task *addstar* [9].

Using *imcore* we created source catalogues for each of the AS images, which we call "output" and compared them to the original source list "input". The ratio of recovered AS to the original 5000 stars for a magnitude range between $12.0 \leq K_s \leq 18.2$ mag is shown in Fig. 11. In the first test (solid lines) we consider a positive AS detection if a source was found within 1 pixel of the inserted position. However, in addition to the simple detection we also need to know with which accuracy the "input" magnitude is recovered. Based on the AS experiments of the "ACS Globular Cluster Survey" (Sarajedini et al. 2007; Anderson et al. 2008) we first allowed a 0.75 mag offset between input and output magnitude, which we finally reduced to 0.5 mag. This is based on the fact that the stellar densities in both our fields are assumed to be significantly lower than that within the central region of a globular cluster, targeted by the ACS Globular Cluster Survey. The completeness curve for those tests is shown in Fig. 11 by dashed lines.

Based on the different completeness pattern we find that the source detection efficiency reaches 50% for stars with $17.8 \lesssim K_s \lesssim 18.1$ mag in field b204, and $16.4 \lesssim K_s \lesssim 16.9$ mag in field b314, respectively, depending on the restrictions applied. We also note that the completeness is somewhat lower for the brightest stars (12.0 to 12.2 mag) in both fields. A possible explanation may be that those stars are close to the saturation limit and the photometric accuracy is therefore reduced.

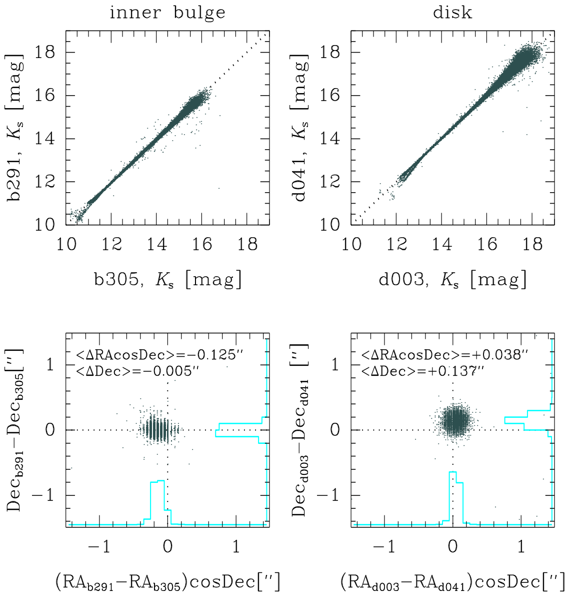

Fig. 10. Top panels: Photometry in the K_s band for the overlapping region between tiles b291 and b305 (left), and d003 and d041 (right). Only stellar sources were used in these plots. Bottom panels: Astrometric accuracy for the same overlapping regions. The mean values for $\Delta\alpha\times\cos\delta$ and $\Delta\delta$ are shown in the top left corner. Counting histograms for the distribution are also shown for both axes.

4. Comparison with 2MASS photometry

The VVV observations are approximately 4 magnitudes deeper than 2MASS. In addition, a very important factor is the excellent image quality (with seeing $0.''9 - 1.''0$) in the entire VVV Survey area for the multi-band, single epoch observations. This allows us to reach the red clump magnitude across the entire bulge (Gonzalez et al. 2011a; Saito et al. 2011), and therefore to study the stellar populations and the structure of the inner Galaxy to an unprecedented level of detail, as for example, identification of RR Lyrae and derivation of accurate distances. Figure 12 shows a CMD for $10' \times 10'$ regions in the inner bulge (b305) and the outer bulge (b235) of VVV stellar sources compared to 2MASS CMDs of the same regions. As the VVV photometry is much deeper it allows us not only to trace the red clump even in the most extincted regions, but also to study the stellar populations behind the bulge. A detailed study of the colour transformations between VISTA and 2MASS photometric systems for VVV disk fields will be presented by Soto et al. (2011, in prep.).

5. VVV DR1 catalogues vs. PSF photometry

The photometric catalogues published in this, as well as any following VVV data release, are based on aperture photometry only, computed by the CASU pipeline on individual tiles (see Section 2.4). However, for very crowded fields (e.g., the innermost Galactic Centre or the central region of stellar clusters), more complete and deeper photometry can be obtained with PSF photometry. In this section we present tests performed by VVV team members using PSF photometry on the VVV images. The results show that the PSF fitting can reach up to 1.5 mag deeper than aperture photometry, detecting up to twice more sources for highly crowded fields, where aperture photometry is known to be inefficient, particularly for faint sources. We emphasize that the PSF data are not part of the VVV DR1.

The tests were performed using the *apermag3* aperture fluxes, that are used in the CASU catalogues as well as in the VSA database as the default values to represent the flux for all

---

[9] IRAF is distributed by the National Optical Astronomy Observatories, which are operated by the Association of Universities for Research in Astronomy, Inc., under cooperative agreement with the US National Science Foundation.

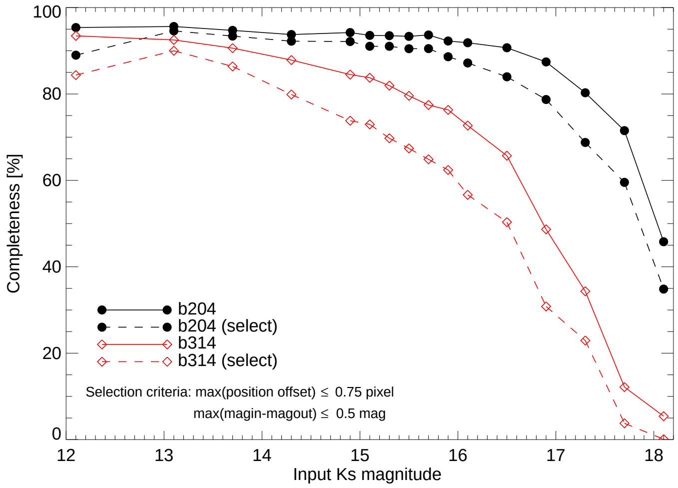

Fig. 11. K_s band completeness test for two 2000×2000 pixels^2 $(11\overset{\prime}{.}3 \times 11\overset{\prime}{.}3)$ fields from the bulge area of the VVV Survey. The fields were selected to represent a less crowded region (tile b204) as well as one of the most crowded regions near the Galactic Centre (tile b314). Solid points correspond to b204, whereas open diamonds represent b314. In addition we apply selection criteria to define a confirmed source detection in our AS experiments (see text for details). Solid lines show the completeness fraction if a source was detected within a radius ≤ 1 pixel of its original position. Reducing this radius to 0.5 pixel and requiring the original K_s band magnitude to be recovered within 0.5 mag results in the completeness curves shown with dashed lines.

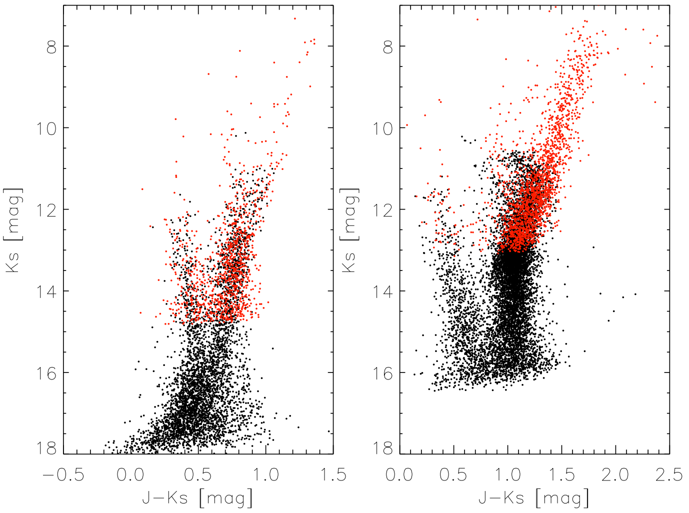

Fig. 12. CMDs comparing VVV (black) and 2MASS data (red) for the bulge area. The left-hand panel shows a field in the outer bulge (b235) while the right-hand panel shows one of the most crowded bulge fields (b305), close to the Galactic Centre.

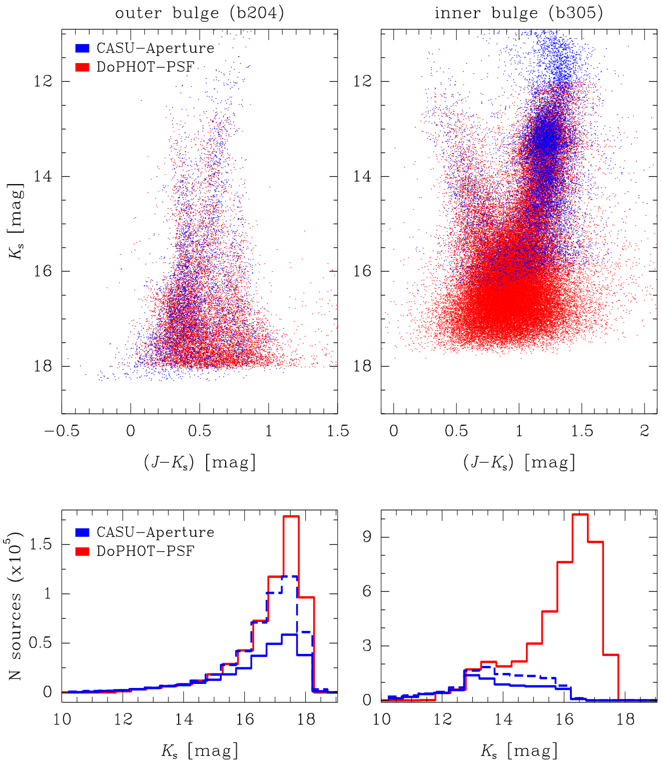

Fig. 13. The top-left panel shows a K_s *vs.* $(J - K_s)$ CMD for a less crowded bulge field (a section of tile b204) comparing the 5σ magnitude limit of the CASU aperture photometry with PSF photometry (also with 5σ magnitude limit). The bottom-left panel shows histograms for all sources (dashed line) and only the stellar objects (solid line) found in tile b204, also in comparison with the PSF photometry. The right-hand panels show the same analysis for a highly crowded field close to the Galactic Centre (tile b305).

images. However, the CASU pipeline measures positions and fluxes for different concentric apertures designed to adequately sample the curve-of-growth of the majority of images. The *apermag1* has $1''$ diameter and each successive aperture increases by a factor of $\sqrt{2}$ in diameter. For highly crowded fields the aperture photometry using the *apermag3* can simultaneously fit multiple overlapping sources, but it does not perform any subtraction in order to check for fainter sources hidden underneath. In this case the *apermag1* and *apermag2* can be more suitable than *apermag3*, even taking into account that small apertures have more uncertain aperture corrections, especially in poor seeing conditions.

Figure 13 shows in the top-left panel the K_s *vs.* $(J - K_s)$ CMD for a field with relatively low crowding and extinction (a section of tile b204), comparing aperture photometry performed by CASU with PSF photometry obtained with DoPHOT (Schechter et al. 1993) for the same field, using 5σ magnitude limits in both cases. All structures are correctly seen in both cases, and both aperture and PSF photometries reach $K_s \sim 18.0$ mag.

The bottom-left panel of Fig. 13 shows the magnitude distribution of all sources found in the CASU catalogue (dashed line) as well as of stellar sources only (solid line). Even taking into account that aperture photometry contain some brighter stars that are not present in the PSF photometry, the total number of sources found by PSF photometry in the K_s band image of b204 is 589, 187, in comparison to 482, 004 (all sources) and 273, 550 (stellar flag) sources present in the CASU catalogue.

For comparison, the same analysis is performed in the right panel of Fig. 13 for the inner bulge field b305, where the effects

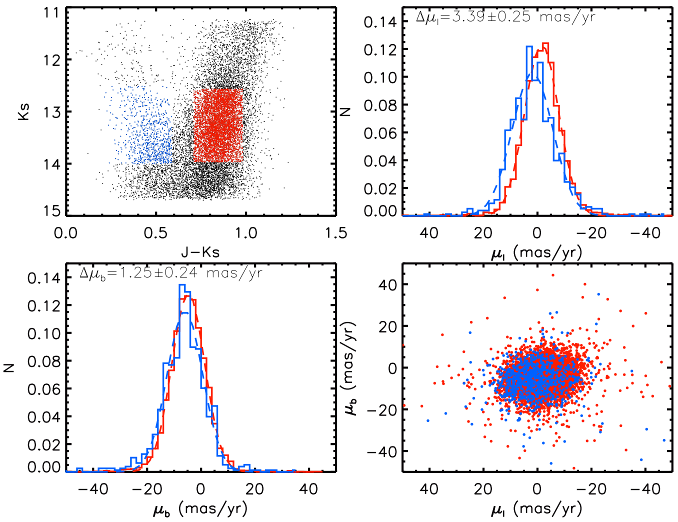

Fig. 14. Top left panel: K_s *vs.* $(J - K_s)$ CMD for a 10 × 10 arcmin^2 region in tile b249 for VVV stellar sources matched with 2MASS. The CMD is centred in the region of the bulge red clump (red) and the disk main sequence (blue). Top right panel: histogram of the longitudinal proper motion for both selected regions in the CMD. The mean values for $\Delta\alpha\times\cos\delta$ and $\Delta\delta$ are shown in the top left corner. Bottom left panel: same as top right panel for the latitudinal proper motion distribution. Bottom right panel: the μ_b *vs.* μ_l distribution in units of mas yr^{-1}.

of crowding and extinction are significant. PSF photometry allows us not only to resolve the high density areas, but it also reaches ~ 1.5 mag deeper, i.e., $K_s \sim 17.5$ mag, while the aperture photometry is limited to $K_s \sim 16.0$ mag. The bottom-right panel of Fig. 13 shows how much the PSF photometry exceeds the aperture photometry for faint sources. The total number of sources found by PSF photometry for field b305 in the K_s band is 4, 601, 529 in comparison to 1, 201, 557, (all flags) and 818, 706 (stellar only) sources present in the CASU catalogue.

Tests performed by VVV team members show that the PSF photometry can be even deeper using a DAOPHOT-ALLFRAME suite of routines (Stetson 1994) customized for the VVV data (Mauro et al. 2011, in prep.).

6. Astrometry

The native VISTA WCS distortion model for pawprints is based on Zenith-Pole-North (ZPN) projection and is available in image headers. The distortions are radial and are well described by:

$$r' = k_1 \times r + k_3 \times r^3 + k_5 \times r^5, \qquad (1)$$

with $k_1 = 0.3413$ arcsec/pix being the plate scale at the centre, and $k_3/k_1 = 44$, $k_5/k_1 = 10{,}300$ are distortion coefficients in angular units of radians. Higher order terms are negligible.

The median WCS *rms* is ~ 70 mas and is dominated by the 2MASS astrometric errors. We note that in both coadded pawprints as well as complete tiles the pixels have been resampled to a common spatial scale and the astrometric distortions have been removed according to equation (1). The resampling was also required in the pawprints since the jitter offsets are sufficiently large (i.e., 15.″0) to affect the coadding (see also Table 3), due to the size of the distortions. Another way to evaluate the internal astrometric accuracy is to use overlaps between different tiles. Hundreds of stars are detected independently on two adjacent tiles. Fig. 10 shows in the top panels the photometry in K_s for overlapping regions between tiles in the inner bulge (b291 and b305) and disk (d003 and d041) areas. Different observing strategies, in particular exposure times (see Table 3), for the disk and bulge areas, as well as the high background brightness due to unresolved stars in the inner bulge, make the bulge photometry shallower than that in the disk region. The astrometric accuracy is shown in the bottom panels of Fig. 10 in terms of the distribution $\Delta\delta$ *vs.* $\Delta\alpha\times\cos\delta$. Typical values for the astrometric accuracy are ~ 25 mas for a $K_s = 15.0$ mag source and ~ 175 mas for $K_s = 18.0$ mag. Despite the shorter time baseline of the VVV Survey, the typical proper motion measurements should reach the accuracy between ~ 7 mas yr^{-1} ($K_s = 15.0$ mag) to ~ 15 mas yr^{-1} ($K_s = 18.0$ mag) after the five years of the VVV campaign.

A test for such measurements can already be achieved using 2MASS and VVV datasets which provide a time baseline of 11 years. Cross-matching of sources between VVV and 2MASS was performed for a 10 × 10 arcmin^2 field in tile b249. The astrometric differences between stellar sources in these two catalogues can be used to derive proper motions of stars in terms of μ_l and μ_b. Clarkson et al. (2008), based on two epochs of HST imaging, showed that foreground disk stars observed in the colour-magnitude diagrams towards the bulge can be separated based on Gaussian fits to the distribution of their proper motions with mean differences of $(\Delta\mu_l, \Delta\mu_b) = (3.22 \pm 0.15, 0.81 \pm 0.13)$ mas yr^{-1}.

Figure 14 shows the selection of stars in the CMD for matched stars between VVV and 2MASS which belong to disk and bulge populations together with the distribution of μ_l and μ_b for each selection. Although the distributions are wider than those presented in the HST analysis of Clarkson et al. (2008), the mean differences between proper motions of disk and bulge are still evident based on these data showing differences of $(\Delta\mu_l, \Delta\mu_b) = (3.39 \pm 0.25, 1.25 \pm 0.24)$ mas yr^{-1}, in good agreement with those of Clarkson et al. (2008).

7. VVV Source maps

Figures 15 and 16 show all objects with stellar flag detected in each tile in the DR1 data. Only stars matched in the J, H and K_s filters have been plotted. The total number of sources found in the bulge region is 7.06×10^7, while the disk has 9.29×10^7 sources. The stellar density (corrected for the total field size) is higher in the disk due to the deeper photometry in all five filters in comparison to the bulge observations (see Table 3, and Figs. 3, 4 and 5).

Note that these density maps already provide a wealth of information on the extinction and the structure of the inner Galaxy, which will be investigated in detail in subsequent papers (e.g., Gonzalez et al. 2011a,b, Saito et al. 2011, in prep.).

The regular grid pattern seen in both the bulge and disk areas is due to the overlap of adjacent tiles. The individual catalogues used in Figs. 15 and 16 contain ~ 10% of the total number of sources twice, contributed by two independent tiles, and leading to the much higher source density shown in both figures. The detection of a significant percentage of sources on two independent tiles not only helps to test and/or confirm the photometric and astrometric calibration, but also to carry out quality control. These density maps are also used to identify problematic tiles, i.e., incomplete data readouts, missing tiles and observations taken under strongly varying seeing conditions (e.g., tiles b216 and b343).

Moreover, those overlap regions will also be beneficial for one of the main scientific goals of the VVV Survey. Since the different tiles are observed independently (with the exception of concatenated tiles), the variable stars included on those tiles will obtain twice as many the K_s epochs, and hence much better sampled light curves (see also Catelan et al. 2011).

8. Difference image testing

Whilst DR1 does not include photometry based on difference image analysis (DIA) we have tested the suitability of the data for DIA analysis based on a modified double-pass version of the ISIS package Alard & Lupton (1998) originally developed for the Angstrom M31 microlensing survey (Kerins et al. 2010).

Currently the VVV Science Verification (SV) field comprises the largest number of epochs and therefore most DIA testing has been performed on this dataset. One issue with difference imaging of VVV data is that often the seeing is so good that the point spread function (PSF) is poorly sampled by the pixel size of around $0\farcs34$. For good DIA kernel convolution we usually require upwards of 2.5 pixels/FWHM. In order to minimize undersampling, instead of convolving a good seeing reference image to a poorer seeing target we select a poor seeing reference frame and convolve the target image to it. The DIA image is therefore constructed by minimizing

$$D^2_{i,j} = \min \sum_{i,j} [R_{i,j} - (T \otimes K)_{i,j} + B_{i,j}]^2, \qquad (2)$$

where the sum is over pixel coordinates (i, j), R and T are the reference and target images, B describes the differential background between R and T, K is the convolution kernel and D is the resulting difference image (see Alard & Lupton (1998) for details of how K is constructed). Prior to difference imaging we add the sky images back onto the sky-subtracted image stacks.

Figure 17 shows a K_S band pawprint from one epoch of the VVV SV bulge field. The lower row shows the resulting difference images. Whilst the difference image quality is reasonably clean there are many black residuals occurring around the many saturated stars in the field. However, variable objects are easy to pick out as in the circled example in the zoomed DIA panel in Fig. 17.

The background noise level of the DIA images is consistent across all arrays and performs well with respect to *imcore* sky noise estimates (Irwin et al. 2004). In Fig. 18 we plot the pixel histograms of DIA flux for the same SV pawprint shown in Fig. 17 for each of the 16 arrays. The fluxes are normalised to a level which is just 40% of the sky noise estimate reported by *imcore*. In all cases the histograms show that difference imaging noise is significantly below that predicted by *imcore*, as evidenced by the close resemblance of the normalised DIA flux distributions to a unit Gaussian curve.

The photometric performance of VVV DIA will be calibrated in further detail in a future paper.

9. Summary

We have presented the VVV Data Release 1, describing the design, observations, data processing, data quality and limitations. The data are of very high quality, and represent a vast improvement over existing near-IR photometry, and are therefore useful for a wide variety of studies of: open/embedded clusters (Borissova et al. 2011; Baume et al. 2011), globular clusters (Minniti et al. 2011a; Moni Bidin et al. 2011), distance scale (Majaess et al. 2011), YSO censuses (Faimali et al. 2011, in prep.), brown dwarfs (Folkes et al. 2011, in prep.), proper motions (Minniti et al. 2011, in prep.), disk stellar populations and variable stars (Pietrukowicz et al. 2011), Galactic structure of the disk mapping the edge of the stellar disk (Minniti et al. 2011b), and the inner structure of the bulge (Gonzalez et al. 2011b), bulge stellar populations including metallicity, extinction and dust maps (Gonzalez et al. 2011a, Catelan et al. 2011

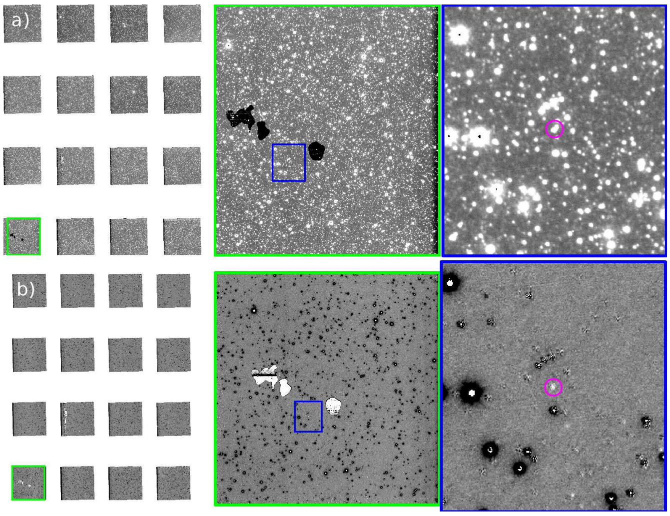

Fig. 17. (a) A K_s band pawprint from one VVV SV bulge field epoch showing views of: the full pawprint (left); a zoom into Array 1 (middle); and a further zoom centred on a circled variable object (right). (b) The bottom row shows the respective difference image views. Blackened objects are DIA residuals around saturated stars, which comprise a non-negligible fraction of the image area for bulge fields.

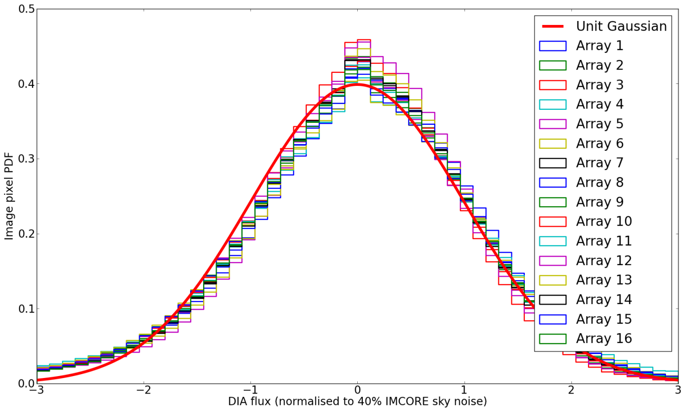

Fig. 18. Noise histograms for the K_s band DIA images shown in row (b) of Fig. 17. The x-axis is difference flux normalised to 40% of the sky noise level reported by *imcore*. The smooth function is a unit Gaussian, which indicates that for this image DIA noise is reasonably Gaussian for all arrays and is characterised by a noise level which is well below the *imcore* sky noise estimate.

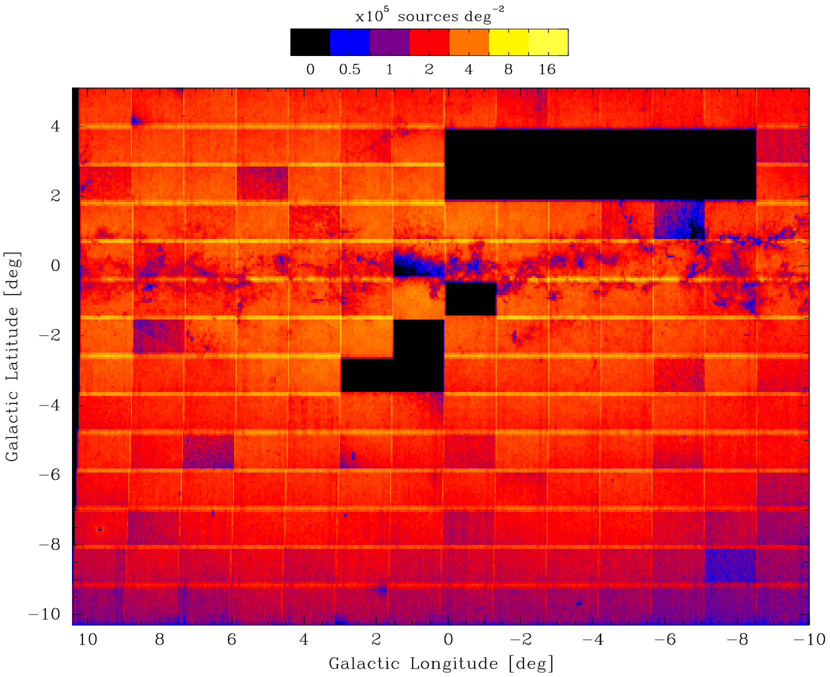

Fig. 15. Density map in logarithmic scale showing the VVV bulge area. The map was made using all the stellar point sources detected in the J, H and K_s 1.1 CASU catalogues. Crowded areas appear in yellow, while less populated regions as well as high extinction areas are shown in blue. The overlapping regions between the tiles are highlighted since the point sources are detected twice, therefore generating the grid pattern, that indicates also the size of overlap regions. The density, in units of 10^5 sources deg^{-2}, is indicated in the horizontal bar at the top.

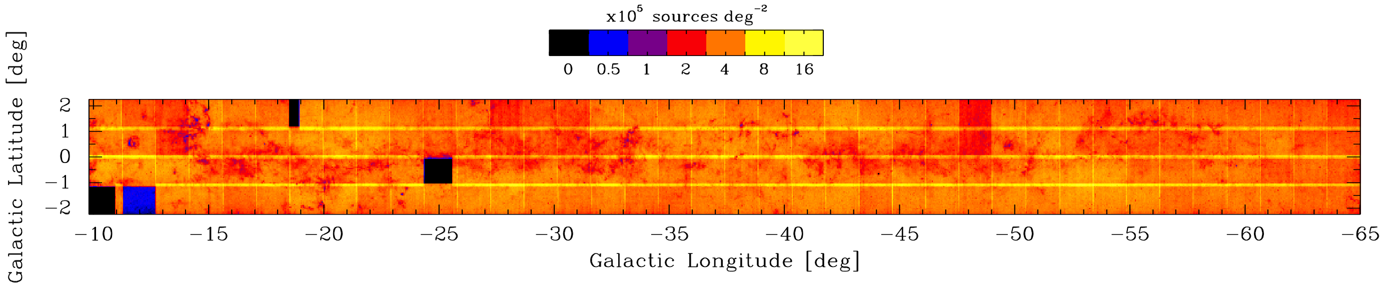

Fig. 16. Density map in logarithmic scale showing the VVV disk area. The notation is similar to that presented in Fig. 15.

in prep)[10] high-energy sources (Greiss et al. 2011a,b, Masetti et al. 2011, in prep.), background galaxies (Amôres et al. 2011, in prep.), color transformations between VISTA and 2MASS systems (Soto et al. 2011, in prep.), as well as enabling and complementing other Galactic structure and stellar population studies, variable star studies in clusters and in the field (pulsating variables, eclipsing binaries and planetary transits), gravitational microlensing studies, Galactic Centre studies, ultra-high-velocity star searches, PNe searches, SN light echo searches, QSO searches, searches for faint Solar System objects (e.g., NEOs, MBAs, LJ5s, TNOs), etc.

Acknowledgements. We gratefully acknowledge use of data from the ESO Public Survey programme ID 179.B-2002 taken with the VISTA telescope, data products from the Cambridge Astronomical Survey Unit, and funding from the FONDAP Center for Astrophysics 15010003, the BASAL CATA Center for Astrophysics and Associated Technologies PFB-06, the FONDECYT from CONICYT, and the Ministry for the Economy, Development, and Tourism's Programa Iniciativa Científica Milenio through grant P07-021-F, awarded to The Milky Way Millennium Nucleus. RKS and DM acknowledge financial support from CONICYT through Gemini Project No. 32080016. DM acknowledge support by Proyecto FONDECYT Regular No. 1090213. MZ and OAG acknowledge support by Proyecto FONDECYT Regular No. 1110393. JB and FP are supported by FONDECYT Regular No. 1080086. JRAC is supported by CONICYT through Gemini Project No. 32090002. ANC received support from Comitee Mixto ESO-Gobierno de Chile. MS acknowledges support by Proyecto FONDECYT Regular No. 3110188 and Comite Mixto ESO-Gobierno de Chile. Support for RA is provided by Proyecto FONDECYT Regular No. 3100029. RdG acknowledges partial research support through grant 11073001 from the National Natural Science Foundation of China. MMH is supported for

---

[10] The Bulge Extinction and Metallicity calculator based on VVV maps is available at: `http://www.eso.org/~ogonzale/BEAMEC/calculator.php`

this work by the US National Science Foundation under Grant No. 0607497 and 1009550. GP acknowledge support from the Millennium Center for Supernova Science through grant P06-045-F funded by Programa Bicentenario de Ciencia y Tecnologa de CONICYT. MC, JAG and ID acknowledge support by Proyecto FONDECYT Regular No. 1110326. MC is also supported in part by Proyecto Anillo ACT-86. SLF acknowledges funding support from the ESO-Government of Chile Mixed Committee 2009 and from the Gemini–CONICYT grant No. 32090014/2009. BB, BD and LSJ acknowledge support from FAPESP and CNPq. EBA thanks Fundação para a Ciência e Tecnologia (FCT) under the grant SFRH/BPD/42239/2007. RK acknowledges support from the Centro de Astrofisica de Valparaiso and Proyecto DIUV23/2009.

References

Alard, C. & Lupton, R., 1998, ApJ, 503, 325
Alcock, C., Allsman, R. A., Alves, D. R., et al. 2000, ApJ, 541, 734
Amôres, E. B., & Lépine, J. R. D. 2005, AJ, 130, 659
Anderson, J., Sarajedini, A., Bedin, L. R., et al. 2008, AJ, 135, 2055
Arnaboldi, M., Neeser, M. J., Parker, L. C., et al. 2007, The Messenger, 127, 28
Baume, G., Carraro, G., Comeron, F., & de Elía, G. C. 2011, A&A, 531, A73
Benjamin, R. A., Churchwell, E., Babler, B. L., et al. 2003, PASP, 115, 953
Borissova, J., Bonatto, C., Kurtev, R., et al. 2011, A&A, 532, A131
Cardelli, J. A., Clayton, G. C., & Mathis, J. S. 1989, ApJ, 345, 245
Catelan, M., Minniti, D., Lucas, P. W., et al. 2011, RR Lyrae Stars, Metal-Poor Stars, and the Galaxy, 145
Cioni, M.-R. L., Clementini, G., Girardi, L., et al. 2011, A&A, 527, A116
Clarkson, W., Sahu, K., Anderson, J., et al. 2008, ApJ, 684, 1110
Cutri, R. M., Skrutskie, M. F., van Dyk, S., et al. 2003, The IRSA 2MASS All-Sky Point Source Catalog, NASA/IPAC Infrared Science Archive
Dalton, G. B., Caldwell, M., Ward, A. K., et al. 2006, Proc. SPIE, 6269,
Dobashi, K., Uehara, H., Kandori, R., et al. 2005, PASJ, 57, 1
Drimmel, R., Cabrera-Lavers, A., & López-Corredoira, M. 2003, A&A, 409, 205
Emerson, J. P., & Sutherland, W. J. 2010, Proc. SPIE, 7733
Epchtein, N., de Batz, B., Copet, E., et al. 1994, Ap&SS, 217, 3
Froebrich, D., Ray, T. P., Murphy, G. C., & Scholz, A. 2005, A&A, 432, L67
Gonzalez, O. A., Rejkuba, M., Zoccali, M., Valenti, E., & Minniti, D. 2011a, A&A, 534, A3
Gonzalez, O. A., Rejkuba, M., Minniti, D., et al. 2011b, A&A, 534, L14
Greiss, S., Steeghs, D., Maccarone, T. J., Jonker, P. G., Torres, M. A. P., Gonzalez, O. A., Masetti, N., & Rojas, A. 2011a, Astronomer's Telegram, 3562
Greiss, S., Steeghs, D., Maccarone, T. J., Hynes, R. I., Britt, C. T., Jonker, P. G., Torres, M. A. P., Masetti, N., Rojas, A., Heinke, C., Kaur, R., & Bird, T. 2011b, Astronomer's Telegram, 3695
Hilker, M., Primas, F., Comerón, F. 2011, Survey Area Definition Tool Cookbook for VISTA
Hodgkin, S. T., Irwin, M. J., Hewett, P. C., & Warren, S. J. 2009, MNRAS, 394, 675
Irwin, M. J., Lewis, J., Hodgkin, S., et al. 2004, Proc. SPIE, 5493, 411
Ivanov, V. D. & Szeifert, T. 2009, VIRCAM/VISTA User Manual
Kerins, E. et al., 2010, MNRAS, 409, 247
Lewis, J. R., Irwin, M., & Bunclark, P. 2010, Astronomical Data Analysis Software and Systems XIX, 434, 91
Lucas, P. W., Hoare, M. G., Longmore, A., et al. 2008, MNRAS, 391, 136
Majaess, D., Turner, D., Moni Bidin, C., et al. 2011, ApJ, 741, L27
Marshall, D. J., Robin, A. C., Reylé, C., Schultheis, M., & Picaud, S. 2006, A&A, 453, 635
Minniti, D., Lucas, P. W., Emerson, J. P., et al. 2010, New A, 15, 433
Minniti, D., Hempel, M., Toledo, I., et al. 2011a, A&A, 527, A81
Minniti, D., Saito, R. K., Alonso-García, J., Lucas, P. W., & Hempel, M. 2011b, ApJ, 733, L43
Moni Bidin, C., Mauro, F., Geisler, D., et al. 2011, arXiv:1109.1854
Nagayama, T., Nagashima, C., Nakajima, Y., et al. 2003, Proc. SPIE, 4841, 459
Nishiyama, S., Nagata, T., Sato, S., et al. 2006, ApJ, 647, 1093
Nishiyama, S., Tamura, M., Hatano, H., et al. 2009, ApJ, 696, 1407
Pietrukowicz, P., Minniti, D., Alonso-Garcia, J., & Hempel, M. 2011, arXiv:1110.3453
Saito, R., Hempel, M., Alonso-García, J., et al. 2010, The Messenger, 141, 24
Saito, R. K., Zoccali, M., McWilliam, A., et al. 2011, AJ, 142, 76
Sarajedini, A., Bedin, L. R., Chaboyer, B., et al. 2007, AJ, 133, 1658
Schechter, P. L., Mateo, M., & Saha, A. 1993, PASP, 105, 1342
Schlegel, D. J., Finkbeiner, D. P., & Davis, M. 1998, ApJ, 500, 525
Stetson, P. B. 1994, PASP, 106, 250
Taylor, M. B. 2006, Astronomical Data Analysis Software and Systems XV, 351, 666
Udalski, A., Szymanski, M., Kaluzny, J., Kubiak, M., & Mateo, M. 1993, Acta Astron., 43, 69

---

[1] Departamento Astronomía y Astrofísica, Pontificia Universidad Católica de Chile, Av. Vicuña Mackenna 4860, Santiago, Chile
[2] Vatican Observatory, Vatican City State V-00120, Italy
[3] Department of Astrophysical Sciences, Princeton University, Princeton, NJ 08544-1001, USA
[4] Centre for Astrophysics Research, University of Hertfordshire, College Lane, Hatfield AL10 9AB, UK
[5] European Southern Observatory, Karl-Schwarzschild-Strasse 2, D-85748 Garching, Germany
[6] Atacama Large Millimeter Array, Alonso de Córdova 3107, Vitacura, Santiago, Chile
[7] Institute of Astronomy, University of Cambridge, Madingley Road, Cambridge CB3 0HA, UK
[8] Institute for Astronomy, The University of Edinburgh, Royal Observatory, Blackford Hill, Edinburgh EH9 3HJ, UK
[9] European Southern Observatory, Ave. Alonso de Cordova 3107, Casilla 19, Santiago 19001, Chile
[10] Jodrell Bank Centre for Astrophysics, The University of Manchester, Oxford Road, Manchester M13 9PL, UK
[11] Astronomy Unit, School of Physics and Astronomy, Queen Mary University of London, Mile End Road, London, E1 4NS, UK
[12] Departamento de Física, Universidad de La Serena, Cisternas 1200 Norte, La Serena, Chile
[13] Faculdade de Ciências da Universidade de Lisboa, Campo Grande, Edificio C5, 1749-016 Lisboa, Portugal
[14] Laboratório Nacional de Astrofísica, Rua Estados Unidos 154, Itajubá-MG, 37504-364, Brazil
[15] Instituto de Astronomía Teórica y Experimental, CONICET, Laprida 922, 5000 Córdoba, Argentina
[16] Centro de Astro-Ingeniería, Pontificia Universidad Católica de Chile, Av. Vicuña Mackenna 4860, Santiago, Chile
[17] INAF - Osservatorio Astronomico di Bologna, via Ranzani 1, 40127, Bologna
[18] Warsaw University Observatory, Al. Ujazdowskie 4,00-478, Warsaw, Poland
[19] Departmento de Astronomía, Universidad de Concepción, Casilla 160-C, Concepción, Chile
[20] Departamento de Física y Astronomía, Facultad de Ciencias, Universidad de Valparaíso, Ave. Gran Bretaña 1111, Playa Ancha, Casilla 5030, Valparaíso, Chile
[21] Observatorio Astronómico de Córdoba, Universidad Nacional de Córdoba, Laprida 854, 5000 Córdoba, Argentina
[22] Consejo Nacional de Investigaciones Científicas y Técnicas, Av. Rivadavia 1917 - CPC1033AAJ - Buenos Aires, Argentina
[23] Gemini Observatory, Southern Operations Center, c/o AURA, Casilla 603 La Serena, Chile
[24] Department of Astronomy, University of Florida, 211 Bryant Space Science Center P.O. Box 112055, Gainesville, FL, 32611-2055, USA
[25] Instituto de Ciencias Astronómicas, del la Tierra y del Espacio (ICATE-CONICET), Av. España Sur 1512, J5402DSP San Juan, Argentina
[26] Universidade de São Paulo, IAG, Rua do Matão 1226, Cidade Universitária, São Paulo 05508-900, Brazil
[27] Facultad de Ciencias Astronómicas y Geofísicas, Universidad Nacional de La Plata, and Instituto de Astrofísica La Plata (IALP–CONICET), Paseo del Bosque S/N, B1900FWA, La Plata, Argentina
[28] INAF - Astronomical Observatory of Padova, vicolo dell Osservatorio 5, I - 35122 Padova, Italy
[29] Dipartimento di Astronomia, Universitá di Padova, vicolo dell Osservatorio 3, 35122 Padova, Italy
[30] Department of Physics, University of Wisconsin-Whitewater, 800 West Main Street, Whitewater, WI 53190
[31] Universidade Federal do Rio Grande do Sul, IF, CP 15051, Porto Alegre 91501-970, RS, Brazil
[32] Departamento de Astronomía, Universidad de Chile, Casilla 36-D, Santiago, Chile

[33]Kavli Institute for Astronomy and Astrophysics, Peking University, Yi He Yuan Lu 5, Hai Dian District, Beijing 100871, China
[34]Department of Astronomy and Space Science, Kyung Hee University, Yongin-shi, Kyungki-do 449-701, Republic of Korea
[35]Max Planck Institute for Astronomy, Königstuhl 17, 69117 Heidelberg, Germany
[36]Departamento de Física, Ingeniería de Sistemas y Teoría de la Señal, Universidad de Alicante, Apdo. 99, E03080 Alicante, Spain
[37]Mullard Space Science Laboratory, University College London, Holmbury St. Mary, Dorking, Surrey, RH5 6NT, UK
[38]Department of Physics, University of Cincinnati, PO Box 210011, Cincinnati, OH 45221-0011, USA
[39]School of Physics & Astronomy, University of Leeds, Woodhouse Lane, Leeds LS2 9JT, UK
[40]NASA-Ames Research Center/Bay Area Environmental Research Institute, MS 244-30, Moffett Field, CA 94035, USA
[41]UK Astronomy Technology Centre, Royal Observatory, Blackford Hill, Edinburgh EH9 3HJ
[42]Instituto de Astrofísica de Canarias, Vía Láctea s/n, E38205 - La Laguna (Tenerife), Spain
[43]Departamento de Astrofísica, Universidad de La Laguna, E-38206, La Laguna, Tenerife, Spain
[44]School of Physics and Astronomy, University of Southampton, Highfield, Southampton, SO17 1BJ, UK
[45]Saint Marys University, 923 Robie Street, Halifax, Nova Scotia, Canada
[46]Centro de Astrobiologia CSIC - INTA, Carretera Torrejón-Ajalvir km 4, 28850, Madrid, Spain
[47]Istituto di Astrofisica Spaziale e Fisica Cosmica di Bologna, via Gobetti 101, 40129 Bologna, Italy
[48]Service d'Astrophysique - IRFU, CEA-Saclay, 91191 Gif sur Yvette, France
[49]Instituto de Astronomía y Física del Espacio, Casilla de Correo 67, Sucursal 28, Buenos Aires, Argentina
[50]Department of Physics & Astronomy, Macquarie University, Sydney, NSW 2109, Australia
[51]Australian Astronomical Observatory, PO Box 296, Epping, NSW 1710, Australia
[52]Departamento de Ciencias Fisicas, Universidad Andres Bello, Av. Republica 252, Santiago, Chile
[53]South African Astronomical Observatory, PO Box 9, Observatory 7935, Cape Town, South Africa
[54]Hartebeesthoek Radio Astronomy Observatory, PO Box 443, Krugersdorp 1740, South Africa
[55]Aryabhatta Research Institute of Observational Sciences (ARIES), Manora Peak, 263 129 Nainital, India
[56]The University of Kent, Canterbury, Kent, CT2 7NH, UK
[57]Gemini Observatory, Northern Operations Center, 670 N. A'ohoku Place, Hilo, Hawaii, 96720, USA
[58]Division of Optical and Infrared Astronomy, National Astronomical Observatory of Japan 2-21-1 Osawa, Mitaka, Tokyo, 181-8588, Japan
[59]Departamento de Ingeniería Eléctrica, Pontificia Universidad Católica de Chile, Av. Vicuña Mackenna 4860, Santiago, Chile

Appendix A: VVV Tile coordinates

Here we list the tile centre coordinates for all VVV pointings. There are 196 bulge tiles, with names starting with ”b”, and 152 tiles in the disk area, having names starting with ”d”. For each tile we provide tile centre coordinates in Equatorial and Galactic coordinates. All tiles have been observed using the identical offsetting strategy, combining 6 pawprints to contiguously fill 1.5 × 1.1 sq. deg area. The second last column lists the filters for which the tile has been completed (i.e., observed within constraints), and the last column lists the number of epochs taken in K_s band within the first observing season (DR1).

Table A.1. VVV Tile centres.

Tile name	RA (J2000.0) dd:mm:ss.sss	DEC (J2000.0) dd:mm:ss.ss	longitude degrees	latitude degrees	Filters completed	K_s epochs completed
d001	11:43:24.936	−63:31:38.64	295.43770	−1.64975	$ZYJHK_s$	5
d002	11:56:12.576	−63:52:21.00	296.89672	−1.64979	$ZYJHK_s$	5
d003	12:09:17.184	−64:08:46.68	298.35572	−1.64971	$ZYJHK_s$	5
d004	12:22:35.184	−64:20:48.12	299.81470	−1.64971	$ZYJHK_s$	5
d005	12:36:02.640	−64:28:18.84	301.27373	−1.64973	$ZYJHK_s$	5
d006	12:49:35.184	−64:31:14.88	302.73271	−1.64977	$ZYJHK_s$	5
d007	13:03:08.352	−64:29:34.44	304.19170	−1.64978	$ZYJHK_s$	5
d008	13:16:37.632	−64:23:18.24	305.65072	−1.64970	$ZYJHK_s$	5
d009	13:29:58.632	−64:12:30.24	307.10972	−1.64971	JHK_s	5
d010	13:43:07.272	−63:57:15.84	308.56873	−1.64973	$ZYJHK_s$	5
d011	13:55:59.856	−63:37:42.60	310.02772	−1.64971	$ZYJHK_s$	5
d012	14:08:33.240	−63:14:00.24	311.48673	−1.64970	$ZYJHK_s$	5
d013	14:20:44.808	−62:46:19.92	312.94573	−1.64979	$ZYJHK_s$	5
d014	14:32:32.496	−62:14:52.80	314.40472	−1.64974	$ZYJHK_s$	5
d015	14:43:42.144	−61:40:33.96	315.83598	−1.64972	$ZYJHK_s$	4
d016	14:54:38.784	−61:02:16.44	317.29497	−1.64975	$ZYJHK_s$	4
d017	15:05:08.712	−60:20:51.00	318.75395	−1.64975	$ZYJHK_s$	4
d018	15:15:11.880	−59:36:30.60	320.21293	−1.64975	$ZYJHK_s$	4
d019	15:24:48.600	−58:49:27.84	321.67194	−1.64978	$ZYJHK_s$	4
d020	15:33:59.400	−57:59:54.60	323.13095	−1.64976	$ZYJHK_s$	4
d021	15:42:45.072	−57:08:02.40	324.58996	−1.64971	$ZYJHK_s$	4
d022	15:51:06.576	−56:14:02.40	326.04898	−1.64975	$ZYJHK_s$	4
d023	15:59:04.920	−55:18:04.32	327.50799	−1.64974	$ZYJHK_s$	5
d024	16:06:41.208	−54:20:17.88	328.96694	−1.64974	$ZYJHK_s$	5
d025	16:13:56.640	−53:20:51.36	330.42599	−1.64974	$ZYJHK_s$	5
d026	16:20:52.320	−52:19:53.40	331.88495	−1.64978	$ZYJHK_s$	5
d027	16:27:29.400	−51:17:30.84	333.34393	−1.64976	JHK_s	2
d028	16:33:49.032	−50:13:50.52	334.80299	−1.64976	JHK_s	2
d029	16:39:52.248	−49:08:58.92	336.26199	−1.64971	JHK_s	2
d030	16:45:40.128	−48:03:01.80	337.72099	−1.64973	$ZYJHK_s$	2
d031	16:51:13.632	−46:56:04.20	339.17999	−1.64971	$ZYJHK_s$	2
d032	16:56:33.720	−45:48:11.16	340.63896	−1.64975	$ZYJHK_s$	2
d033	17:01:41.256	−44:39:26.64	342.09795	−1.64972	$ZYJHK_s$	1
d034	17:06:37.104	−43:29:54.96	343.55695	−1.64975	$ZYJHK_s$	1
d035	17:11:22.032	−42:19:39.72	345.01595	−1.64979	$ZYJHK_s$	1
d036	17:15:56.760	−41:08:44.16	346.47495	−1.64979	JHK_s	1
d037	17:20:21.984	−39:57:11.16	347.93400	−1.64973	JHK_s	1
d038	17:24:38.352	−38:45:04.32	349.39294	−1.64975	JHK_s	1
d039	11:45:52.488	−62:28:17.40	295.43747	−0.55759	$ZYJHK_s$	5
d040	11:58:14.160	−62:48:15.12	296.89617	−0.55758	$ZYJHK_s$	5
d041	12:10:50.928	−63:04:04.80	298.35479	−0.55753	$ZYJHK_s$	5
d042	12:23:39.672	−63:15:39.60	299.81350	−0.55756	$ZYJHK_s$	5
d043	12:36:36.744	−63:22:53.40	301.27213	−0.55754	$ZYJHK_s$	5
d044	12:49:38.376	−63:25:42.96	302.73081	−0.55755	$ZYJHK_s$	5
d045	13:02:40.560	−63:24:06.84	304.18948	−0.55760	$ZYJHK_s$	5
d046	13:15:39.288	−63:18:05.40	305.64814	−0.55754	$ZYJHK_s$	5
d047	13:28:30.696	−63:07:42.24	307.10682	−0.55756	JHK_s	5
d048	13:41:11.112	−62:53:02.04	308.56549	−0.55756	JHK_s	5
d049	13:53:37.224	−62:34:12.00	310.02413	−0.55760	$ZYJHK_s$	5
d050	14:05:46.176	−62:11:20.04	311.48283	−0.55756	$ZYJHK_s$	5
d051	14:17:35.520	−61:44:36.60	312.94152	−0.55757	$ZYJHK_s$	5
d052	14:29:03.312	−61:14:12.48	314.40014	−0.55761	$ZYJHK_s$	5
d053	14:40:08.135	−60:40:18.48	315.85883	−0.55752	$ZYJHK_s$	4
d054	14:50:49.032	−60:03:07.56	317.31750	−0.55758	$ZYJHK_s$	4
d055	15:01:05.424	−59:22:51.24	318.77616	−0.55761	$ZYJHK_s$	4
d056	15:10:57.120	−58:39:41.40	320.23482	−0.55759	$ZYJHK_s$	3
d057	15:20:24.264	−57:53:49.92	321.69349	−0.55755	$ZYJHK_s$	4
d058	15:29:27.264	−57:05:28.32	323.15217	−0.55754	$ZYJHK_s$	4
d059	15:38:06.720	−56:14:47.40	324.61087	−0.55755	$ZYJHK_s$	4
d060	15:46:23.352	−55:21:57.60	326.06950	−0.55754	$ZYJHK_s$	4

Table A.1. continued.

Tile name	RA (J2000.0) dd:mm:ss.sss	DEC (J2000.0) dd:mm:ss.ss	longitude degrees	latitude degrees	Filters completed	K_{s} epochs completed
d061	15:54:18.096	−54:27:08.64	327.52817	−0.55761	$ZYJHK_{\mathrm{s}}$	5
d062	16:01:51.840	−53:30:29.16	328.98684	−0.55756	$ZYJHK_{\mathrm{s}}$	5
d063	16:09:05.616	−52:32:08.16	330.44549	−0.55755	$ZYJHK_{\mathrm{s}}$	5
d064	16:16:00.456	−51:32:13.20	331.90419	−0.55754	$ZYJHK_{\mathrm{s}}$	5
d065	16:22:37.368	−50:30:51.84	333.36286	−0.55756	JHK_{s}	2
d066	16:28:57.360	−49:28:10.56	334.82153	−0.55755	JHK_{s}	2
d067	16:35:01.416	−48:24:15.84	336.28015	−0.55756	JHK_{s}	2
d068	16:40:50.520	−47:19:13.08	337.73882	−0.55761	$ZYJHK_{\mathrm{s}}$	2
d069	16:46:25.560	−46:13:07.32	339.19753	−0.55758	$ZYJHK_{\mathrm{s}}$	2
d070	16:51:47.400	−45:06:03.96	340.65613	−0.55757	$ZYJHK_{\mathrm{s}}$	2
d071	16:56:56.928	−43:58:06.96	342.11483	−0.55761	$ZYJHK_{\mathrm{s}}$	1
d072	17:01:54.864	−42:49:20.28	343.57351	−0.55754	$ZYJHK_{\mathrm{s}}$	1
d073	17:06:42.000	−41:39:48.24	345.03215	−0.55756	$ZYJHK_{\mathrm{s}}$	1
d074	17:11:19.032	−40:29:33.72	346.49083	−0.55759	JHK_{s}	1
d075	17:15:46.608	−39:18:39.96	347.94953	−0.55759	JHK_{s}	1
d076	17:20:05.328	−38:07:09.84	349.40822	−0.55752	JHK_{s}	1
d077	11:48:10.080	−61:24:47.16	295.43749	0.53461	$ZYJHK_{\mathrm{s}}$	5
d078	12:00:07.584	−61:44:03.84	296.89636	0.53458	$ZYJHK_{\mathrm{s}}$	5
d079	12:12:18.648	−61:59:20.40	298.35521	0.53456	$ZYJHK_{\mathrm{s}}$	5
d080	12:24:40.392	−62:10:30.00	299.81408	0.53461	$ZYJHK_{\mathrm{s}}$	5
d081	12:37:09.600	−62:17:27.96	301.27295	0.53465	$ZYJHK_{\mathrm{s}}$	5
d082	12:49:42.840	−62:20:11.40	302.73182	0.53458	$ZYJHK_{\mathrm{s}}$	5
d083	13:02:16.560	−62:18:38.16	304.19066	0.53466	$ZYJHK_{\mathrm{s}}$	5
d084	13:14:47.232	−62:12:50.04	305.64955	0.53458	$ZYJHK_{\mathrm{s}}$	5
d085	13:27:11.328	−62:02:48.84	307.10837	0.53460	$ZYJHK_{\mathrm{s}}$	4
d086	13:39:25.632	−61:48:39.24	308.56725	0.53465	$ZYJHK_{\mathrm{s}}$	4
d087	13:51:27.144	−61:30:28.08	310.02613	0.53456	$ZYJHK_{\mathrm{s}}$	5
d088	14:03:13.176	−61:08:22.20	311.48497	0.53458	$ZYJHK_{\mathrm{s}}$	5
d089	14:14:41.544	−60:42:30.60	312.94386	0.53465	$ZYJHK_{\mathrm{s}}$	4
d090	14:25:50.400	−60:13:03.72	314.40272	0.53463	$ZYJHK_{\mathrm{s}}$	4
d091	14:36:38.352	−59:40:11.64	315.86159	0.53462	$ZYJHK_{\mathrm{s}}$	4
d092	14:47:04.392	−59:04:05.52	317.32043	0.53461	$ZYJHK_{\mathrm{s}}$	4
d093	14:57:07.920	−58:24:56.16	318.77932	0.53465	$ZYJHK_{\mathrm{s}}$	3
d094	15:06:48.648	−57:42:55.44	320.23818	0.53459	$ZYJHK_{\mathrm{s}}$	3
d095	15:16:06.552	−56:58:13.80	321.69700	0.53459	$ZYJHK_{\mathrm{s}}$	5
d096	15:25:01.920	−56:11:02.04	323.15588	0.53461	$ZYJHK_{\mathrm{s}}$	5
d097	15:33:35.208	−55:21:30.60	324.61479	0.53459	$ZYJHK_{\mathrm{s}}$	4
d098	15:41:46.968	−54:29:49.20	326.07365	0.53465	$ZYJHK_{\mathrm{s}}$	4
d099	15:49:37.968	−53:36:07.56	327.53250	0.53463	$ZYJHK_{\mathrm{s}}$	4
d100	15:57:09.024	−52:40:34.32	328.99135	0.53458	$ZYJHK_{\mathrm{s}}$	4
d101	16:04:20.976	−51:43:17.40	330.45023	0.53459	$ZYJHK_{\mathrm{s}}$	5
d102	16:11:14.736	−50:44:24.72	331.90911	0.53460	$ZYJHK_{\mathrm{s}}$	5
d103	16:17:51.216	−49:44:03.48	333.36798	0.53460	$ZYJHK_{\mathrm{s}}$	3
d104	16:24:11.328	−48:42:20.16	334.82687	0.53461	$ZYJHK_{\mathrm{s}}$	3
d105	16:30:15.960	−47:39:21.24	336.28568	0.53460	$ZYJHK_{\mathrm{s}}$	3
d106	16:36:06.000	−46:35:12.12	337.74450	0.53460	$ZYJHK_{\mathrm{s}}$	3
d107	16:41:42.312	−45:29:57.84	339.20338	0.53460	JHK_{s}	1
d108	16:47:05.712	−44:23:43.44	340.66229	0.53457	JHK_{s}	1
d109	16:52:16.944	−43:16:33.24	342.12118	0.53461	JHK_{s}	1
d110	16:57:16.776	−42:08:31.56	343.58005	0.53462	$ZYJHK_{\mathrm{s}}$	1
d111	17:02:05.904	−40:59:42.36	345.03883	0.53459	$ZYJHK_{\mathrm{s}}$	1
d112	17:06:45.024	−39:50:08.52	346.49771	0.53457	$ZYJHK_{\mathrm{s}}$	1
d113	17:11:14.736	−38:39:53.28	347.95664	0.53461	$ZYJHK_{\mathrm{s}}$	2
d114	17:15:35.640	−37:29:00.24	349.41546	0.53460	$ZYJHK_{\mathrm{s}}$	2
d115	11:50:18.720	−60:21:09.00	295.43768	1.62680	$ZYJHK_{\mathrm{s}}$	5
d116	12:01:53.760	−60:39:47.52	296.89732	1.62677	$ZYJHK_{\mathrm{s}}$	5
d117	12:13:40.992	−60:54:32.75	298.35689	1.62684	$ZYJHK_{\mathrm{s}}$	5
d118	12:25:37.800	−61:05:19.68	299.81648	1.62674	$ZYJHK_{\mathrm{s}}$	5
d119	12:37:41.304	−61:12:02.52	301.27608	1.62684	$ZYJHK_{\mathrm{s}}$	5
d120	12:49:48.408	−61:14:39.48	302.73567	1.62683	$ZYJHK_{\mathrm{s}}$	5

Table A.1. continued.

Tile name	RA (J2000.0) dd:mm:ss.sss	DEC (J2000.0) dd:mm:ss.ss	longitude degrees	latitude degrees	Filters completed	K_s epochs completed
d121	13:01:55.944	−61:13:09.12	304.19526	1.62680	$ZYJHK_\mathrm{s}$	5
d122	13:14:00.720	−61:07:32.15	305.65484	1.62675	$ZYJHK_\mathrm{s}$	5
d123	13:25:59.640	−60:57:50.40	307.11447	1.62681	$ZYJHK_\mathrm{s}$	4
d124	13:37:49.704	−60:44:08.88	308.57402	1.62675	$ZYJHK_\mathrm{s}$	4
d125	13:49:28.248	−60:26:32.28	310.03361	1.62680	$ZYJHK_\mathrm{s}$	5
d126	14:00:52.872	−60:05:08.16	311.49324	1.62678	$ZYJHK_\mathrm{s}$	5
d127	14:12:01.440	−59:40:04.44	312.95280	1.62677	$ZYJHK_\mathrm{s}$	4
d128	14:22:52.272	−59:11:29.76	314.41240	1.62684	$ZYJHK_\mathrm{s}$	4
d129	14:33:24.024	−58:39:34.56	315.87197	1.62678	$ZYJHK_\mathrm{s}$	4
d130	14:43:35.688	−58:04:28.20	317.33156	1.62679	$ZYJHK_\mathrm{s}$	4
d131	14:53:26.616	−57:26:21.48	318.79117	1.62676	$ZYJHK_\mathrm{s}$	3
d132	15:02:56.424	−56:45:24.48	320.25077	1.62679	$ZYJHK_\mathrm{s}$	3
d133	15:12:05.040	−56:01:48.00	321.71037	1.62674	$ZYJHK_\mathrm{s}$	5
d134	15:20:52.560	−55:15:41.76	323.16993	1.62676	$ZYJHK_\mathrm{s}$	5
d135	15:29:19.344	−54:27:15.48	324.62955	1.62682	$ZYJHK_\mathrm{s}$	4
d136	15:37:25.872	−53:36:39.24	326.08912	1.62676	$ZYJHK_\mathrm{s}$	4
d137	15:45:12.720	−52:44:01.32	327.54872	1.62676	$ZYJHK_\mathrm{s}$	4
d138	15:52:40.584	−51:49:30.36	329.00835	1.62678	$ZYJHK_\mathrm{s}$	4
d139	15:59:50.184	−50:53:14.64	330.46790	1.62680	$ZYJHK_\mathrm{s}$	5
d140	16:06:42.360	−49:55:21.36	331.92752	1.62681	$ZYJHK_\mathrm{s}$	5
d141	16:13:17.904	−48:55:57.72	333.38714	1.62678	$ZYJHK_\mathrm{s}$	3
d142	16:19:37.608	−47:55:10.20	334.84670	1.62678	$ZYJHK_\mathrm{s}$	3
d143	16:25:42.312	−46:53:04.92	336.30624	1.62678	$ZYJHK_\mathrm{s}$	3
d144	16:31:32.832	−45:49:46.92	337.76590	1.62684	$ZYJHK_\mathrm{s}$	3
d145	16:37:09.936	−44:45:22.32	339.22547	1.62682	$ZYJHK_\mathrm{s}$	1
d146	16:42:34.392	−43:39:55.44	340.68506	1.62681	JHK_s	1
d147	16:47:46.920	−42:33:30.96	342.14462	1.62677	JHK_s	1
d148	16:52:48.216	−41:26:12.48	343.60424	1.62683	JHK_s	1
d149	16:57:38.976	−40:18:04.32	345.06387	1.62680	$ZYJHK_\mathrm{s}$	1
d150	17:02:19.800	−39:09:10.08	346.52343	1.62677	$ZYJHK_\mathrm{s}$	1
d151	17:06:51.312	−37:59:32.64	347.98303	1.62675	$ZYJHK_\mathrm{s}$	2
d152	17:11:14.064	−36:49:15.24	349.44260	1.62674	$ZYJHK_\mathrm{s}$	2
b201	18:04:24.384	−41:44:53.52	350.74816	−9.68974	$ZYJHK_\mathrm{s}$	1
b202	18:08:00.144	−40:27:29.88	352.22619	−9.68971	$ZYJHK_\mathrm{s}$	1
b203	18:11:29.496	−39:09:52.92	353.70409	−9.68973	$ZYJHK_\mathrm{s}$	1
b204	18:14:52.992	−37:52:03.36	355.18207	−9.68974	$ZYJHK_\mathrm{s}$	1
b205	18:18:11.136	−36:34:02.64	356.66012	−9.68976	$ZYJHK_\mathrm{s}$	1
b206	18:21:24.360	−35:15:52.20	358.13813	−9.68975	$ZYJHK_\mathrm{s}$	1
b207	18:24:33.096	−33:57:33.48	359.61607	−9.68977	$ZYJHK_\mathrm{s}$	2
b208	18:27:37.728	−32:39:07.20	1.09399	−9.68974	$ZYJHK_\mathrm{s}$	2
b209	18:30:38.640	−31:20:34.08	2.57200	−9.68971	$ZYJHK_\mathrm{s}$	2
b210	18:33:36.168	−30:01:55.56	4.04998	−9.68973	$ZYJHK_\mathrm{s}$	2
b211	18:36:30.624	−28:43:12.36	5.52796	−9.68978	$ZYJHK_\mathrm{s}$	2
b212	18:39:22.272	−27:24:25.20	7.00593	−9.68975	$ZYJHK_\mathrm{s}$	3
b213	18:42:11.424	−26:05:34.80	8.48396	−9.68974	$ZYJHK_\mathrm{s}$	2
b214	18:44:58.320	−24:46:42.24	9.96193	−9.68974	$ZYJHK_\mathrm{s}$	3
b215	17:59:15.960	−41:13:55.92	350.74595	−8.59756	$ZYJHK_\mathrm{s}$	1
b216	18:02:55.992	−39:57:07.92	352.21956	−8.59753	$ZYJHK_\mathrm{s}$	1
b217	18:06:29.472	−38:40:04.08	353.69327	−8.59756	$ZYJHK_\mathrm{s}$	1
b218	18:09:56.880	−37:22:46.56	355.16684	−8.59757	$ZYJHK_\mathrm{s}$	1
b219	18:13:18.768	−36:05:16.07	356.64051	−8.59760	$ZYJHK_\mathrm{s}$	1
b220	18:16:35.568	−34:47:34.08	358.11423	−8.59759	$ZYJHK_\mathrm{s}$	1
b221	18:19:47.688	−33:29:42.36	359.58781	−8.59757	$ZYJHK_\mathrm{s}$	2
b222	18:22:55.560	−32:11:41.28	1.06151	−8.59755	$ZYJHK_\mathrm{s}$	2
b223	18:25:59.544	−30:53:32.28	2.53522	−8.59757	$ZYJHK_\mathrm{s}$	2
b224	18:28:59.952	−29:35:16.80	4.00880	−8.59759	$ZYJHK_\mathrm{s}$	2
b225	18:31:57.120	−28:16:54.84	5.48250	−8.59755	$ZYJHK_\mathrm{s}$	2
b226	18:34:51.360	−26:58:27.84	6.95620	−8.59757	$ZYJHK_\mathrm{s}$	3
b227	18:37:42.912	−25:39:56.88	8.42977	−8.59756	$ZYJHK_\mathrm{s}$	2
b228	18:40:32.088	−24:21:21.96	9.90350	−8.59757	$ZYJHK_\mathrm{s}$	3

Table A.1. continued.

Tile name	RA (J2000.0) dd:mm:ss.sss	DEC (J2000.0) dd:mm:ss.ss	longitude degrees	latitude degrees	Filters completed	K_s epochs completed
b229	17:54:12.456	−40:42:07.56	350.74383	−7.50542	$YJHK_s$	1
b230	17:57:56.496	−39:25:54.48	352.21380	−7.50537	JHK_s	–
b231	18:01:33.792	−38:09:24.48	353.68363	−7.50537	JHK_s	1
b232	18:05:04.920	−36:52:38.28	355.15359	−7.50541	JHK_s	1
b233	18:08:30.312	−35:35:38.04	356.62342	−7.50539	JHK_s	1
b234	18:11:50.472	−34:18:24.48	358.09337	−7.50535	JHK_s	1
b235	18:15:05.832	−33:00:59.76	359.56322	−7.50542	JHK_s	2
b236	18:18:16.752	−31:43:24.24	1.03312	−7.50538	$ZYJHK_s$	2
b237	18:21:23.640	−30:25:39.36	2.50307	−7.50541	$ZYJHK_s$	2
b238	18:24:26.808	−29:07:46.20	3.97300	−7.50540	JHK_s	2
b239	18:27:26.568	−27:49:45.84	5.44287	−7.50536	JHK_s	2
b240	18:30:23.256	−26:31:39.36	6.91271	−7.50540	JHK_s	2
b241	18:33:17.136	−25:13:27.12	8.38261	−7.50541	JHK_s	3
b242	18:36:08.472	−23:55:10.20	9.85251	−7.50542	JHK_s	2
b243	17:49:13.848	−40:09:29.16	350.74206	−6.41324	$YJHK_s$	1
b244	17:53:01.608	−38:53:51.72	352.20875	−6.41323	JHK_s	–
b245	17:56:42.504	−37:37:54.84	353.67546	−6.41323	JHK_s	1
b246	18:00:17.064	−36:21:40.32	355.14219	−6.41321	JHK_s	1
b247	18:03:45.792	−35:05:09.96	356.60888	−6.41323	JHK_s	1
b248	18:07:09.120	−33:48:25.20	358.07550	−6.41322	JHK_s	1
b249	18:10:27.504	−32:31:27.12	359.54218	−6.41323	JHK_s	2
b250	18:13:41.328	−31:14:17.16	1.00886	−6.41325	$ZYJHK_s$	2
b251	18:16:50.952	−29:56:56.04	2.47562	−6.41319	JHK_s	2
b252	18:19:56.736	−28:39:25.92	3.94224	−6.41326	JHK_s	2
b253	18:22:58.968	−27:21:46.80	5.40892	−6.41319	JHK_s	2
b254	18:25:58.008	−26:04:00.12	6.87563	−6.41325	JHK_s	2
b255	18:28:54.072	−24:46:06.60	8.34231	−6.41319	JHK_s	3
b256	18:31:47.496	−23:28:07.32	9.80903	−6.41325	JHK_s	2
b257	17:44:20.112	−39:36:02.16	350.74076	−5.32104	JHK_s	1
b258	17:48:11.328	−38:20:59.64	352.20485	−5.32102	JHK_s	1
b259	17:51:55.560	−37:05:36.24	353.66885	−5.32101	JHK_s	–
b260	17:55:33.360	−35:49:53.40	355.13291	−5.32104	JHK_s	–
b261	17:59:05.184	−34:33:52.92	356.59692	−5.32103	JHK_s	–
b262	18:02:31.512	−33:17:36.24	358.06096	−5.32105	JHK_s	–
b263	18:05:52.752	−32:01:04.80	359.52500	−5.32104	JHK_s	–
b264	18:09:09.288	−30:44:20.04	0.98899	−5.32099	JHK_s	–
b265	18:12:21.528	−29:27:23.40	2.45295	−5.32106	JHK_s	–
b266	18:15:29.784	−28:10:15.24	3.91703	−5.32105	JHK_s	–
b267	18:18:34.368	−26:52:57.36	5.38103	−5.32101	JHK_s	–
b268	18:21:35.616	−25:35:30.48	6.84507	−5.32101	JHK_s	–
b269	18:24:33.792	−24:17:55.68	8.30909	−5.32100	JHK_s	1
b270	18:27:29.184	−23:00:14.04	9.77309	−5.32107	$ZYJHK_s$	1
b271	17:39:31.128	−39:01:49.44	350.73953	−4.22883	JHK_s	1
b272	17:43:25.536	−37:47:22.20	352.20141	−4.22884	JHK_s	1
b273	17:47:12.888	−36:32:31.92	353.66332	−4.22886	JHK_s	1
b274	17:50:53.688	−35:17:20.76	355.12516	−4.22890	JHK_s	1
b275	17:54:28.416	−34:01:49.80	356.58709	−4.22886	JHK_s	1
b276	17:57:57.528	−32:46:01.20	358.04898	−4.22882	JHK_s	1
b277	18:01:21.456	−31:29:56.40	359.51088	−4.22881	JHK_s	1
b278	18:04:40.584	−30:13:36.84	0.97275	−4.22884	JHK_s	1
b279	18:07:55.272	−28:57:03.60	2.43463	−4.22884	JHK_s	1
b280	18:11:05.880	−27:40:17.76	3.89659	−4.22886	JHK_s	1
b281	18:14:12.696	−26:23:20.76	5.35849	−4.22883	JHK_s	1
b282	18:17:16.056	−25:06:13.68	6.82039	−4.22886	JHK_s	1
b283	18:20:16.224	−23:48:57.60	8.28222	−4.22888	JHK_s	–
b284	18:23:13.488	−22:31:32.88	9.74416	−4.22889	JHK_s	–
b285	17:34:46.896	−38:26:51.72	350.73871	−3.13666	JHK_s	–
b286	17:38:44.256	−37:12:59.40	352.19896	−3.13670	JHK_s	–
b287	17:42:34.488	−35:58:41.88	353.65931	−3.13670	JHK_s	–
b288	17:46:18.096	−34:44:01.68	355.11962	−3.13673	$ZYJHK_s$	–

Table A.1. continued.

Tile name	RA (J2000.0) dd:mm:ss.sss	DEC (J2000.0) dd:mm:ss.ss	longitude degrees	latitude degrees	Filters completed	K_s epochs completed
b289	17:49:55.536	−33:29:00.24	356.57994	−3.13668	$ZYJHK_s$	1
b290	17:53:27.288	−32:13:39.72	358.04023	−3.13673	$ZYJHK_s$	1
b291	17:56:53.736	−30:58:01.20	359.50054	−3.13672	$ZYJHK_s$	–
b292	18:00:15.264	−29:42:06.12	0.96088	−3.13663	ZY	–
b293	18:03:32.280	−28:25:56.28	2.42120	−3.13666	ZY	–
b294	18:06:45.096	−27:09:32.75	3.88150	−3.13671	$ZYJHK_s$	–
b295	18:09:54.024	−25:52:56.64	5.34179	−3.13672	$ZYJHK_s$	–
b296	18:12:59.352	−24:36:09.00	6.80204	−3.13666	$ZYJHK_s$	–
b297	18:16:01.416	−23:19:10.92	8.26235	−3.13668	$ZYJHK_s$	1
b298	18:19:00.456	−22:02:03.12	9.72271	−3.13666	JHK_s	1
b299	17:30:07.272	−37:51:11.88	350.73789	−2.04453	JHK_s	–
b300	17:34:07.344	−36:37:53.76	352.19711	−2.04451	JHK_s	–
b301	17:38:00.240	−35:24:09.00	353.65635	−2.04453	$ZYJHK_s$	–
b302	17:41:46.440	−34:09:59.40	355.11565	−2.04449	$ZYJHK_s$	–
b303	17:45:26.424	−32:55:27.48	356.57487	−2.04453	$ZYJHK_s$	1
b304	17:49:00.600	−31:40:34.32	358.03411	−2.04446	$ZYJHK_s$	1
b305	17:52:29.424	−30:25:22.08	359.49334	−2.04452	$ZYJHK_s$	–
b306	17:55:53.256	−29:09:51.84	0.95261	−2.04456	$ZYJHK_s$	–
b307	17:59:12.432	−27:54:05.04	2.41186	−2.04451	$ZYJHK_s$	–
b308	18:02:27.312	−26:38:03.12	3.87111	−2.04447	$ZYJHK_s$	–
b309	18:05:38.232	−25:21:47.52	5.33034	−2.04451	$ZYJHK_s$	–
b310	18:08:45.480	−24:05:18.96	6.78962	−2.04454	$ZYJHK_s$	–
b311	18:11:49.320	−22:48:38.52	8.24891	−2.04449	$ZYJHK_s$	1
b312	18:14:50.040	−21:31:47.64	9.70816	−2.04447	JHK_s	1
b313	17:25:32.232	−37:14:49.92	350.73753	−0.95236	JHK_s	1
b314	17:29:34.800	−36:02:05.64	352.19625	−0.95230	JHK_s	1
b315	17:33:30.168	−34:48:52.92	353.65504	−0.95232	JHK_s	1
b316	17:37:18.768	−33:35:14.28	355.11368	−0.95231	JHK_s	1
b317	17:41:01.104	−32:21:10.80	356.57248	−0.95229	JHK_s	1
b318	17:44:37.584	−31:06:45.00	358.03121	−0.95230	JHK_s	1
b319	17:48:08.616	−29:51:58.32	359.48996	−0.95233	JHK_s	1
b320	17:51:34.560	−28:36:52.56	0.94861	−0.95235	JHK_s	1
b321	17:54:55.800	−27:21:28.44	2.40742	−0.95234	JHK_s	1
b322	17:58:12.648	−26:05:48.12	3.86612	−0.95234	JHK_s	1
b323	18:01:25.416	−24:49:52.68	5.32477	−0.95232	JHK_s	1
b324	18:04:34.440	−23:33:42.84	6.78355	−0.95232	JHK_s	1
b325	18:07:39.984	−22:17:20.40	8.24226	−0.95238	JHK_s	–
b326	18:10:42.288	−21:00:45.72	9.70101	−0.95231	JHK_s	–
b327	17:21:01.656	−36:37:48.00	350.73744	0.13984	JHK_s	1
b328	17:25:06.528	−35:25:37.20	352.19621	0.13989	JHK_s	1
b329	17:29:04.152	−34:12:56.52	353.65492	0.13987	JHK_s	–
b330	17:32:55.008	−32:59:47.76	355.11368	0.13984	JHK_s	–
b331	17:36:39.504	−31:46:13.08	356.57236	0.13988	JHK_s	–
b332	17:40:18.120	−30:32:14.28	358.03110	0.13982	JHK_s	–
b333	17:43:51.192	−29:17:52.80	359.48985	0.13988	JHK_s	–
b334	17:47:19.128	−28:03:10.80	0.94855	0.13988	JHK_s	–
b335	17:50:42.288	−26:48:09.36	2.40731	0.13985	JHK_s	–
b336	17:54:00.984	−25:32:49.92	3.86610	0.13985	JHK_s	–
b337	17:57:15.528	−24:17:14.28	5.32478	0.13981	JHK_s	–
b338	18:00:26.208	−23:01:23.16	6.78348	0.13983	JHK_s	–
b339	18:03:33.336	−21:45:17.64	8.24226	0.13983	JHK_s	1
b340	18:06:37.152	−20:28:59.16	9.70099	0.13985	$ZYJHK_s$	1
b341	17:16:35.472	−36:00:07.56	350.73765	1.23203	$ZYJHK_s$	1
b342	17:20:42.432	−34:48:30.24	352.19686	1.23205	JHK_s	1
b343	17:24:42.144	−33:36:20.88	353.65613	1.23203	JHK_s	1
b344	17:28:35.040	−32:23:41.64	355.11542	1.23207	JHK_s	1
b345	17:32:21.576	−31:10:35.04	356.57468	1.23205	JHK_s	1
b346	17:36:02.160	−29:57:02.52	358.03399	1.23203	JHK_s	1
b347	17:39:37.152	−28:43:06.24	359.49322	1.23206	JHK_s	1
b348	17:43:06.960	−27:28:47.64	0.95251	1.23203	JHK_s	1

Table A.1. continued.

Tile name	RA (J2000.0) dd:mm:ss.sss	DEC (J2000.0) dd:mm:ss.ss	longitude degrees	latitude degrees	Filters completed	K_s epochs completed
b349	17:46:31.896	−26:14:08.52	2.41172	1.23201	JHK_s	1
b350	17:49:52.296	−24:59:09.96	3.87096	1.23204	JHK_s	1
b351	17:53:08.496	−23:43:53.40	5.33027	1.23202	JHK_s	–
b352	17:56:20.760	−22:28:20.28	6.78955	1.23201	$ZYJHK_\mathrm{s}$	–
b353	17:59:29.376	−21:12:31.68	8.24885	1.23202	$ZYJHK_\mathrm{s}$	–
b354	18:02:34.608	−19:56:29.04	9.70808	1.23199	$ZYJHK_\mathrm{s}$	–
b355	17:12:13.584	−35:21:49.68	350.73827	2.32427	$ZYJHK_\mathrm{s}$	1
b356	17:16:22.488	−34:10:45.12	352.19857	2.32417	ZY	1
b357	17:20:24.096	−32:59:06.36	353.65894	2.32423	ZY	–
b358	17:24:18.888	−31:46:56.64	355.11924	2.32422	ZY	–
b361	17:35:26.472	−28:07:39.36	359.50024	2.32421	ZY	–
b362	17:38:58.008	−26:53:43.80	0.96059	2.32418	$ZYJHK_\mathrm{s}$	–
b363	17:42:24.624	−25:39:25.92	2.42098	2.32420	$ZYJHK_\mathrm{s}$	–
b364	17:45:46.632	−24:24:47.88	3.88124	2.32419	$ZYJHK_\mathrm{s}$	–
b365	17:49:04.368	−23:09:50.40	5.34158	2.32416	$ZYJHK_\mathrm{s}$	–
b366	17:52:18.096	−21:54:34.92	6.80192	2.32418	JHK_s	1
b367	17:55:28.104	−20:39:02.88	8.26224	2.32419	JHK_s	1
b368	17:58:34.656	−19:23:15.00	9.72265	2.32423	JHK_s	1
b369	17:07:55.872	−34:42:57.24	350.73892	3.41637	$ZYJHK_\mathrm{s}$	1
b370	17:12:06.480	−33:32:24.36	352.20083	3.41644	$ZYJHK_\mathrm{s}$	1
b371	17:16:09.864	−32:21:16.20	353.66280	3.41638	$ZYJHK_\mathrm{s}$	–
b372	17:20:06.384	−31:09:35.28	355.12466	3.41637	$ZYJHK_\mathrm{s}$	–
b373	17:23:56.496	−29:57:23.04	356.58663	3.41642	$ZYJHK_\mathrm{s}$	–
b374	17:27:40.584	−28:44:42.36	358.04853	3.41640	$ZYJHK_\mathrm{s}$	–
b375	17:31:19.032	−27:31:34.68	359.51046	3.41635	$ZYJHK_\mathrm{s}$	–
b376	17:34:52.152	−26:18:01.44	0.97243	3.41644	$ZYJHK_\mathrm{s}$	–
b377	17:38:20.328	−25:04:05.16	2.43434	3.41638	$ZYJHK_\mathrm{s}$	–
b378	17:41:43.848	−23:49:46.56	3.89631	3.41638	$ZYJHK_\mathrm{s}$	–
b379	17:45:03.024	−22:35:07.44	5.35828	3.41637	$ZYJHK_\mathrm{s}$	1
b380	17:48:18.120	−21:20:09.24	6.82020	3.41640	$ZYJHK_\mathrm{s}$	1
b381	17:51:29.424	−20:04:53.40	8.28204	3.41640	JHK_s	1
b382	17:54:37.224	−18:49:20.64	9.74399	3.41636	JHK_s	1
b383	17:03:42.216	−34:03:30.60	350.73979	4.50856	$ZYJHK_\mathrm{s}$	1
b384	17:07:54.408	−32:53:29.40	352.20380	4.50857	JHK_s	1
b385	17:11:59.352	−31:42:51.12	353.66783	4.50858	JHK_s	1
b386	17:15:57.480	−30:31:37.92	355.13195	4.50860	JHK_s	1
b387	17:19:49.176	−29:19:52.68	356.59597	4.50856	JHK_s	1
b388	17:23:34.824	−28:07:36.84	358.06004	4.50857	JHK_s	1
b389	17:27:14.784	−26:54:52.56	359.52411	4.50859	JHK_s	1
b390	17:30:45.384	−25:43:05.52	0.96034	4.50854	JHK_s	1
b391	17:34:15.096	−24:29:30.12	2.42444	4.50852	JHK_s	1
b392	17:37:40.080	−23:15:31.32	3.88850	4.50858	JHK_s	1
b393	17:41:00.672	−22:01:10.92	5.35253	4.50853	JHK_s	–
b394	17:44:17.136	−20:46:29.64	6.81666	4.50854	JHK_s	–
b395	17:47:29.736	−19:31:29.28	8.28074	4.50857	$ZYJHK_\mathrm{s}$	–
b396	17:50:38.736	−18:16:11.28	9.74476	4.50855	$ZYJHK_\mathrm{s}$	–